

## ABSTRACT

Title of thesis:       CONNECTIVITY BASED PARCELLATION  
                          AND BRAIN ATLAS GENERATION  
                          – EXTRACTING CONNECTOME INFORMATION  
                          FOR SCHIZOPHRENIA RESEARCH

Qi Wang, Master of Science, 2014

Thesis directed by:  Professor Joseph JaJa  
                          Department of Electrical and Computer Engineering

Traditional brain atlases are mainly based on hand-crafted anatomical structures, not taking into consideration useful connectivity pattern information. In our work, we use diffusion weighted imaging data to incorporate connectivity information into atlas generation. We use the software package FSL to process data to extract the connectivity matrix. The brain parcellation problem is formulated as a min-cut problem on a large, sparse graph. Spectral clustering and an original multi-class Hopfield network (MHN) method are applied to solve the problem, each working with a different analytical framework: MHN works in the diffusion space to generate individual parcellations, while spectral clustering works on standard space averaged connectome to generate group level atlases. Group study of brain images with schizophrenia is conducted, showing significant improvement in accuracy for disease diagnosis using features extracted with the proposed parcellation scheme. Hypothesis tests are performed on local structures to explore possible structural causes of the disease.

CONNECTIVITY BASED PARCELLATION AND BRAIN ATLAS  
GENERATION  
– EXTRACTING CONNECTOME INFORMATION FOR  
SCHIZOPHRENIA RESEARCH

by

Qi Wang

Thesis submitted to the Faculty of the Graduate School of the  
University of Maryland, College Park in partial fulfillment  
of the requirements for the degree of  
Master of Science  
2014

Advisory Committee:  
Professor Joseph JaJa, Chair/Advisor  
Professor Amitabh Varshney  
Professor Rama Chellappa

© Copyright by  
Qi Wang  
2014

## Acknowledgments

I owe my thanks to all the people who helped me through the excellent graduate study years and make this thesis possible.

First of all I'd like to thank my advisor, Professor Joseph JaJa for offering me the opportunity, inspirations, equipment and financial support to work on this interesting and challenging problem. Professor JaJa was always there to help. There was never a time when my ask was unanswered. He was always ready to give timely and comprehensive guidance and feedback to my work. He always took my ideas very seriously and gave me huge encouragement and mental support in the most difficult time of my research. The inspiring discussions we had is an invaluable asset in my memory.

I'd like to thank our collaborators, Dr. Rong Chen and Dr. Edward Herskovits from Radiology department of UM Medical school, for kindly providing their valuable brain image data for us to work with, and for their expertise input on helping us familiarize with the neural image literature. The project wouldn't be a success without their help.

I would also like to express my gratitude to Professor Amitabh Varshney and Professor Rama Chellappa for agreeing to serve on my thesis committee and spend their valuable time reviewing my manuscript.

My colleagues in the group have been cherishable friends and constant supports that helped make my graduate life a wonderful experience. Jing Wu helped me familiarize with the basic tools and working environment in the lab to get started,

and taught me a lot of useful software engineering tricks that facilitated development of my framework. Wenshuai Hou had many fruitful discussions with me on the theoretical side and inspired many of my ideas. Michael Ritter has always been a reliable technical support in our lab, who was ready to help whenever needed.

I would also like to thank the ECE UMIACS staff members who gave me timely technical and administrative support. Helps from Fritz McCall, Melanie Prange, Edna Walker and many others are highly appreciated.

I would like to express my deepest thanks to my family. My mother and father have always been the strongest mental support throughout my career. They were always the most patient listener and stood on my side whatever I chose to pursue. Words cannot express my gratitude to them.

Thanks to all the Professors who I've taken course with, talked with, who broadened my knowledge and inspired my critical thinking.

Thanks to all other people who have helped me through my graduate study, who I fail to mention with my humble memory.

Finally, thank you all and may good luck always be with you!

# Table of Contents

List of Figures	vi
1 Introduction	1
1.1 Overview	1
1.2 Diffusion MRI (dMRI)	3
1.3 DWI Processing Tool - FMRIB Software Library (FSL)	4
1.4 Interacting with NIFTI Data in MATLAB – the MATLAB NIFTI Toolbox	5
1.5 Outline of the Thesis	5
2 Generating the Connectivity Matrix from DWI	8
2.1 Overview	8
2.2 Raw Data	9
2.3 Registration	9
2.3.1 Linear Registration	10
2.3.2 Nonlinear Registration	11
2.3.3 Mask registration	12
2.4 Bayes Modeling of Diffusion Parameters and Probablistic Tractography	13
2.4.1 Diffusion Tensor Imaging (DTI) and BEDPOSTX	15
2.4.2 Probabilistic Tractography	16
2.5 Specific Processing Pipeline for the Schizophrenia Data	16
3 Parcellation of an Individual Connectivity Matrix	19
3.1 Connectivity Profile and the Graph-Cut Formulation	19
3.2 Algorithms for Solving the Graph Cut Problem	22
3.2.1 Spectral Clustering	22
3.2.2 Multi-class Hopfield Network	25
4 Individual Subjects Parcellations and Group Analyses	30
4.1 Growing Individual Brain Parcellations	30
4.2 Group Study of Schizophrenia Patients	31
4.3 Results	31

4.3.1	Visual Scan of Parcellation Results . . . . .	31
4.3.2	Significantly Changed Regions and Connections . . . . .	33
4.3.3	Classification . . . . .	39
4.4	Discussion of Results . . . . .	40
5	Group Atlases	43
5.1	Group Atlases Generation . . . . .	43
5.2	Results . . . . .	45
5.3	Discussion of Results . . . . .	49
6	Connectivity Based Atlases Built from Scratch	51
6.1	Overview . . . . .	51
6.2	Computing the Connectivity Profiles in MNI Space from Data in Diffusion Space . . . . .	52
6.3	Clustering . . . . .	60
6.4	Results and Discussion . . . . .	60
7	Concluding Remarks	65
	Bibliography	67

## List of Figures

2.1	Illustration: a warp field is a field of displacement vectors . . . . .	12
2.2	An example warp field visualized in FSLView . . . . .	13
2.3	Registered white matter mask example . . . . .	14
2.4	Registered grey matter mask example . . . . .	14
3.1	Topology and connection weights of the formulated graph-cut problem	21
3.2	Spectral clustering will corrupt region definitions across subjects . . .	25
3.3	Performances of clustering algorithms on the synthetic graph data. Experiment setup: 7 nodes in each clusters, nodes are connected with probability 0.5, intra-class link weights have distribution of $Gaussian(0.5, 0.5^2)$ , inter-class link weights have distribution of $Gaussian(-0.5, 0.5^2)$ . Hopfield network with simulated annealing performs best in all cases.	29
4.1	Consistent deviations from standard atlas with MHN parcellations . .	32
4.2	Classification performances . . . . .	41
5.1	Group atlas of the schizophrenic group . . . . .	46
5.2	Group atlas of the control group . . . . .	47
5.3	Difference map between two group atlases . . . . .	48
5.4	Voxel-wise group difference distributions . . . . .	48
6.1	Parcellation result with diffusion-to-standard coordinate mapping in- curs “resolution holes” problem . . . . .	56
6.2	“Resolution holes” problem is due to resolution gap and unevenness .	57
6.3	Changing the registration to standard-to-diffusion to avoid resolution holes . . . . .	58
6.4	Pure connectivity based atlas: 5 clusters . . . . .	61
6.5	Pure connectivity based atlas: 10 clusters . . . . .	61
6.6	Pure connectivity based atlas: 15 clusters . . . . .	62
6.7	Pure connectivity based atlas: 20 clusters . . . . .	62
6.8	Pure connectivity based atlas: 25 clusters . . . . .	63
6.9	Pure connectivity based atlas: 30 clusters . . . . .	63

## Chapter 1: Introduction

### 1.1 Overview

The analysis of human brain connectome is gaining increasing popularity in brain researches using MRI and fMRI data. The goal of brain network analysis includes the discovery of global network characteristics (e.g. economic wiring [1], short paths [2,3]), the detection of functional clusters [4,5], and the exploration of novel applications in clinical research [6,7].

One fundamental problem that needs to be addressed before any network or connectivity based analysis is possible is to develop a reasonable definition of the “nodes” in the modeled brain network. Although modern tractography tools can generate large graphs with connectivity values as fine as the resolution of single voxels, it is generally hard to store and process such large graphs, and more importantly is unlikely to generate meaningful results due to the high probability of tractography errors at the microscopic level. The common practice is to use some type of a brain atlas to group voxels into structural/functional homogeneous regions and treat each of these regions as a node in the brain network. A macroscopic view of the brain network is then constructed with the connectivity defined as a certain type of summary connectivity value between all voxels in the corresponding pair of

regions.

Due to the critical role of the atlas in defining a brain network, the choice of atlas is becoming a problem that is gaining increasing attention, though no common consensus about the “right” methodology has been reached. There are generally two main approaches pursued in the literature using: pre-defined anatomical atlases, or randomly generated atlases. Pre-defined anatomical atlases are human-crafted atlases based mostly on cytoarchitecture clues, which do not use any connectivity information. These include the AAL atlas [8], the Harvard-Oxford atlas [9](<http://fsl.fmrib.ox.ac.uk/fsl/fslwiki/Atlases>) the ANIMAL algorithm [10] and many others. Usually the atlases are registered from the standard space to the subjects’ local image spaces, and individual brain networks are then generated using tractography tools. In contrast, random atlases are relatively arbitrarily generated in subjects local spaces [11, 12]. The randomly generated atlases lack a clear functional definition; however, their advantage is that researchers can have more control over the size of the nodes (parcellation regions) and thus can perform systematic study about the impact of network size and resolution.

Neither the pre-defined anatomical atlas nor the random atlas approach are primarily developed for connectome analysis. Therefore it is natural to try to generate a connectivity based atlas. Many works have been done on clustering functional networks based on fMRI (e.g. [13, 14]). Fewer works have been made on generating a connectivity atlas based on anatomical connectivity (e.g. [15, 16]), primarily because it is more difficult to select the appropriate signature for clustering with diffusion weighted imaging (DWI) data, and the large computational burden on analyzing

the network at the resolution of DWI data. Our work belongs to the latter category.

In this thesis we propose methods of connectivity based brain parcellation using DWI data. The parcellation problem is formulated as a graph partitioning problem where the topology of the graph is a uniform spatial grid and the edge weights are modeled as similarity of connectivity profiles of the terminal nodes. The DWI data for our research was collected from schizophrenia patients and a control group of subjects. Using the generated parcellations, group studies are done from several perspectives to explore the structural causes of schizophrenia.

## 1.2 Diffusion MRI (dMRI)

Diffusion MRI is a type of MRI imaging technique that is mainly used to analyze white matter connections [17–19]. The idea is that in addition to baseline MRI scans with homogeneous magnetic field, a pulse of strong magnetic field gradient is applied on a known direction. Another pulse of magnetic field gradient with the same magnitude but in the opposite direction is then applied after a time period called “diffusion time”. When water particles diffuse along the gradient direction, a signal attenuation will be observed. The amount of signal attenuation will be affected by the intensity of water diffusion. Since the intensity of water diffusion can reflect the local directionality of the structure, this method is effective at discovering and determining the direction of neural fibers. Images acquired using dMRI are often called diffusion weighted images (DWI).

### 1.3 DWI Processing Tool - FMRIB Software Library (FSL)

Brain network analysis consists of 3 main parts:

- Individual DWI processing bundle, including the Brain Extraction Tool (BET), registration, diffusion tensor estimation and probabilistic tractography.
- Clustering algorithms.
- Group data summary and statistical analysis.

The primary tool for individual DWI processing bundle is the FSL software developed by the Analysis Group, FMRIB, Oxford, UK [20,21](<http://fsl.fmrib.ox.ac.uk/fsl/fslwiki/>). This is a powerful and widely used tool in the literature for MRI, fMRI and DWI data processing. It has a user friendly interface, yet hundreds of command line calls are available that facilitate integration into bigger processing frameworks, and detailed customization of their functionalities. The software is open-source and written in C++. Some of the parts - such as BEDPOSTX (Bayesian Estimation of Diffusion Parameters Obtained using Sampling Techniques) - have been parallelized to run on clusters of CPUs and GPUs. FSL is also shipped with many standard brain atlases that facilitate analysis ([fsl.fmrib.ox.ac.uk/fsl/fslwiki/Atlases](http://fsl.fmrib.ox.ac.uk/fsl/fslwiki/Atlases)), such as the Harvard-Oxford cortical and subcortical structural atlases [22] and the JHU DTI-based white-matter atlases [23]. The specific functionalities used in data processing will be described in some detail in Chapter 2.

FSL is accompanied by a convenient visualization tool called FSLView (<http://fsl.fmrib.ox.ac.uk/fsl/fslview/>), which works primarily with NIFTI image

data format [24]. It can visualize brain images with three views, generate 3D rendering, overlay images of the same dimensions, conveniently iterate through an image sequence and make a movie out of a image sequence, among many other visualization techniques. Many figures in this thesis are direct snapshots from FSLView.

## 1.4 Interacting with NIFTI Data in MATLAB – the MATLAB NIFTI Toolbox

Since the main parts of the clustering algorithms are written in MATLAB, we need a MATLAB interface to interact with the NIFTI file format. The NIFTI toolbox developed by Jimmy Shen came in handy

(<http://www.mathworks.com/matlabcentral/fileexchange/8797-tools-for-nifti-and-analyze-image>). A compressed NIFTI file (.nii.gz) is loaded into MATLAB as a structure, two fields of which are most important: “hdr”, which stores the meta data information of the image data, such as the resolution of the image (voxel size) and bitwidth of elements; “img”, which is a 3D (for a single volume) or 4D (for a series of volumes) array that stores the actual image data.

## 1.5 Outline of the Thesis

In Chapter 2, the pre-processing pipeline for obtaining the connectivity matrix is introduced. The basic theory and mathematical formulation for several important tools in FSL are described, including registration, Bayes diffusion parameter estimation, and probabilistic tractography. The generated connectivity matrix is the

data foundation of connectivity based parcellation analysis and atlas generation.

Chapter 3 introduces the formulation of the parcellation problem and algorithms used to generate the connectivity based parcellation. The problem is formulated as a graph partitioning problem on a weighted “spatial graph”, with weights derived from the similarity measures of connectivity profiles. Spectral clustering and an original method derived from Hopfield networks are applied to solve this problem.

Chapter 4 describes the application of an analysis framework for the schizophrenia data research. Parcellations are obtained in individual diffusion spaces. Hypothesis tests are performed on each of the specific regions to detect the most significantly changed regions associated with the disease. Classification performance is evaluated with regional volume and connectivity features extracted using the proposed parcellation algorithm and the AAL-90 atlas. Results show significant improvement for the proposed parcellation algorithm.

In Chapter 5 we propose a simple group atlas generation scheme that averages the individual parcellations in the diffusion space, and makes an evaluation of the separability of the two groups with the generated group atlases.

The parcellation generation framework introduced in Chapters 4 and 5 highly relies on a common standard initialization, which may not be a good starting point for connectivity based segmentation. The parcellations are better regarded as a connectivity based “optimization” of an existing brain atlas.

Chapter 6 forgoes such reliance on standard atlas initialization and proposes a method to generate purely connectivity based brain atlases. Connectivity profiles

are acquired in the common standard space so that clustering can be performed on averaged connectivity profiles. The main technical issue is efficient aggregation of a large amount of connectivity data. A hash table was chosen to manage the big data combination problem.

Chapter 7 summarizes the thesis and proposes further research.

## Chapter 2: Generating the Connectivity Matrix from DWI

### 2.1 Overview

The brain network data-mining algorithms work on connectivity matrices that represent the brain network connectivity patterns. Therefore before exploring the use of machine learning techniques, these matrices have to be extracted from raw brain image data. In this chapter, we describe brain data and the FSL tools used in the project as well as the process of extracting the required connectivity matrices.

The raw image data are diffusion weighted images acquired from a schizophrenia patients group and a normal control group. The standard MNI152 T1 weighted image is registered onto each of the individual diffusion images, which is then used to transform the white matter and grey matter atlases into the diffusion spaces. Probabilistic tractography is then applied in the diffusion spaces to get the voxel-wise connectivity matrices, with seed regions delineated by the white matter atlas and target regions by the grey matter atlas. The connectivity matrices obtained constitute the foundation for all the analyses carried out in the following chapters. The registration data will have another important usage in Chapter 6, where we try to combine individual connectivity information in a common standard space.

## 2.2 Raw Data

The dataset used in this project are diffusion weighted images (DWI) of 78 subjects with schizophrenia and 48 normal subjects. Our image data are of NIFTI format. We used FSLView and the MATLAB NIFTI tool to interact with the NIFTI files. From these software tools we read that the voxel size of the acquisition is  $1.7188mm \times 1.7188mm \times 3mm$ . For each subject, 70 image volumes are acquired, 6 of which are with no directional magnetic field enforced, and the other 64 with uniformly distributed diffusion directions. Each volume image has a dimension of  $128 \times 128 \times 52$  or  $128 \times 128 \times 53$  voxels.

## 2.3 Registration

Registration is an important standard preprocessing step for almost all types of MRI image processing. It is a process of determining a transformation between two image spaces, and applying the transformation to get a image aligned to the target space. This is necessary before any group analysis is possible, since subjects' brain images differ in size and are subject to physical variations when the image was acquired. The MNI152 T1-weighted MRI image, which is the nonlinear average of 152 structural images registered to the MNI152 coordinate system (shipped with FSL), is a commonly used standard reference image to align MRI images across subjects.

In this thesis, we will use the terms “diffusion space” or “source space” inter-

changeably to refer to the image space of the raw diffusion weighted imaging data files, and the terms “standard space” or “MNI space” interchangeably to refer to the space of MNI152 T1-weighted image.

### 2.3.1 Linear Registration

The linear registration of an image is represented by an affine transform matrix, applied on the voxel coordinates. Denote the coordinate of a voxel in the source space as  $(x_{src}, y_{src}, z_{src})$ , and the coordinate of a voxel in the standard space as  $(x_{std}, y_{std}, z_{std})$ , an affine transform can be denoted by a  $3 \times 4$  matrix:

$$\begin{bmatrix} x_{std} \\ y_{std} \\ z_{std} \end{bmatrix} = \begin{bmatrix} a_{11} & a_{12} & a_{13} & b_1 \\ a_{21} & a_{22} & a_{23} & b_2 \\ a_{31} & a_{32} & a_{33} & b_3 \end{bmatrix} \begin{bmatrix} x_{src} \\ y_{src} \\ z_{src} \\ 1 \end{bmatrix} = \mathbf{A} \begin{bmatrix} x_{src} \\ y_{src} \\ z_{src} \\ 1 \end{bmatrix} \quad (2.1)$$

Typically integer-value standard space coordinates will be transformed from non-integer source space coordinates. In order to determine the right signal intensity value, certain interpolation techniques need to be used. Suppose the interpolated image is  $I_{reg}$  and the standard reference image is  $I_{std}$ , The registration problem can then be formulated as the problem of determining  $\mathbf{A}$  so that a measure of mis-alignment between the two images  $C(I_{reg}, I_{std})$  is minimized.

$$\underset{\mathbf{A}}{\text{minimize}} C(I_{reg}, I_{std}) \quad (2.2)$$

Typical choices of  $C(\cdot, \cdot)$  include least squares, negative normalized correlation,

negative mutual information, etc [25].

The full affine transform matrix provides 12 degrees of freedom, which are scalings in three directions, rotations in three directions, translations in three directions, and skews in three directions. FSL linear registration tool (FLIRT) also provides options for partial degrees of freedom for different purposes. For example, the Rigid Body option (6 degrees of freedom including rotations and translations) can be used for within-subject registration, and the Global Rescale option (7 degrees of freedom including rotations, translations and a common scaling factor along three axes) can be used for within-subject registration when scanner drifting is present.

### 2.3.2 Nonlinear Registration

Nonlinear deformation from the standard structure is so common in individual brains that linear registration is usually not used for cross subject studies. A nonlinear transformation is represented by a warp field, and is formulated by replacing the shift components  $b_1, b_2, b_3$  by values that are specific to each voxel:

$$\begin{bmatrix} x_{std,i} \\ y_{std,i} \\ z_{std,i} \end{bmatrix} = \begin{bmatrix} a_{11} & a_{12} & a_{13} & b_{1,i} \\ a_{21} & a_{22} & a_{23} & b_{2,i} \\ a_{31} & a_{32} & a_{33} & b_{3,i} \end{bmatrix} \begin{bmatrix} x_{src} \\ y_{src} \\ z_{src} \\ 1 \end{bmatrix} = [\mathbf{A}_1 \mathbf{b}_i] \begin{bmatrix} x_{src} \\ y_{src} \\ z_{src} \\ 1 \end{bmatrix} \quad (2.3)$$

that is, there are as many parameters in the warp field as voxels in the target image space - the warp field and the target space have the same resolution. The vector  $\mathbf{b}_i$  is called the displacement vector of the corresponding voxel. An illustration

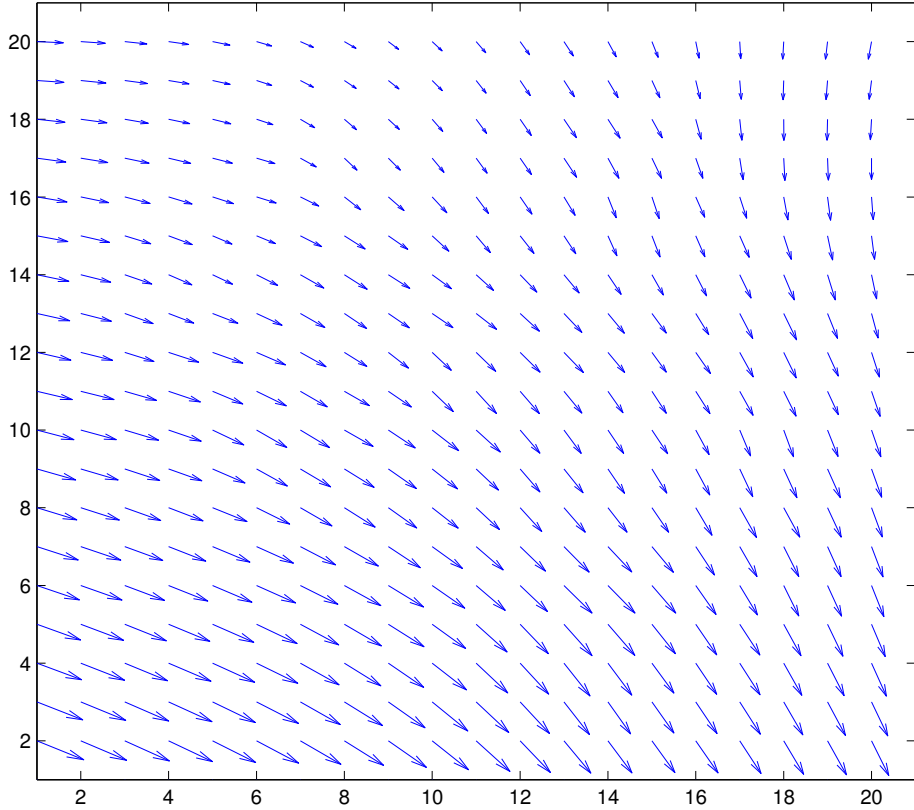


Figure 2.1: Illustration: a warp field is a field of displacement vectors

and a real world example of warp field visualized in FSLView is shown in Figure 2.1 and Figure 2.2, respectively.

### 2.3.3 Mask registration

As will be clear later, a major role of registration in our project is to transform several mask images between spaces: JHU white matter atlas is registered to diffusion spaces to serve as seed regions for probabilistic tractography; AAL-90 atlas is registered to diffusion spaces to serve as target regions on which to compute the con-

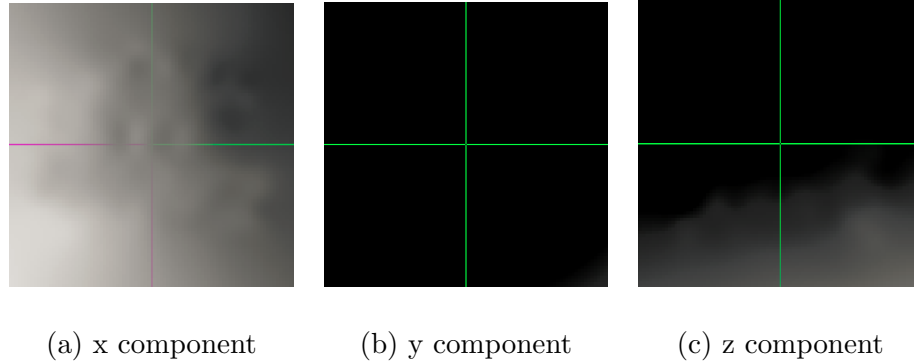


Figure 2.2: An example warp field visualized in FSLView

nectivity matrix, and each of the 90 regions is registered separately to serve as the initialization of the clustering algorithm. When a transform is applied to a binary mask image, the target image will consist of mostly binary-value voxels with a few boundary points having real values between 0 and 1. Simple thresholding is applied to convert these voxels to binary values. Example of registered white matter seed region and grey matter target region is shown in Figures 2.3 and 2.4 respectively, overlaid onto the raw non-diffusion MRI image.

## 2.4 Bayes Modeling of Diffusion Parameters and Probabilistic Tractography

The connectivity matrix of a brain is obtained by performing tractography on the DWI images and counting the number of streamlines connecting each pair of voxels in the target region. In this section we briefly introduce the mathematical modeling of diffusion tensor imaging (DTI) and how FSL uses this model to estimate the diffusion parameters and performs tractography.

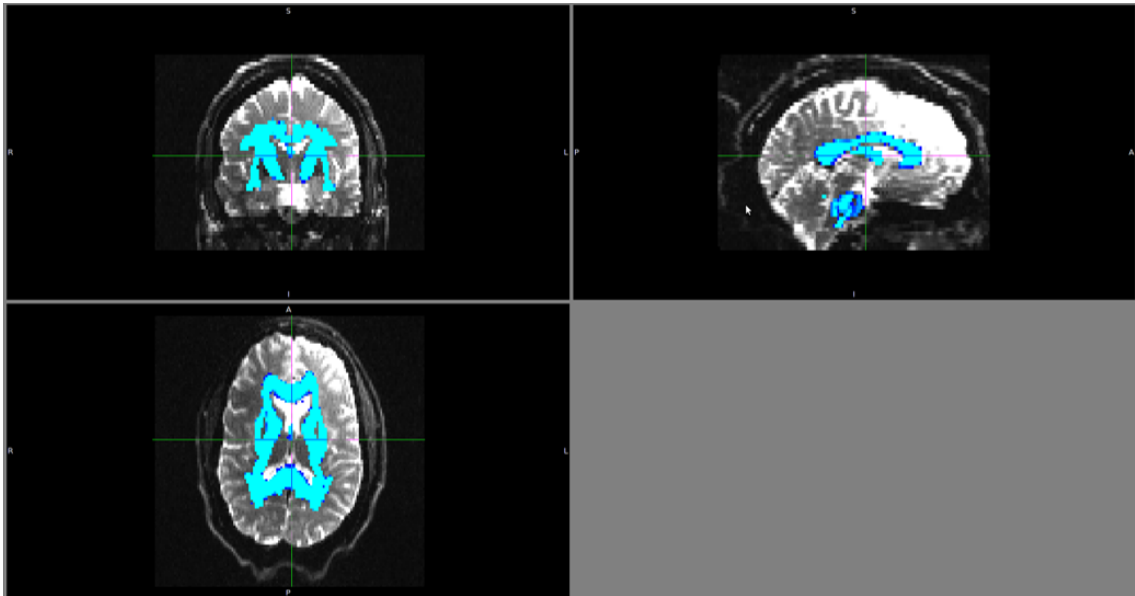


Figure 2.3: Registered white matter mask example

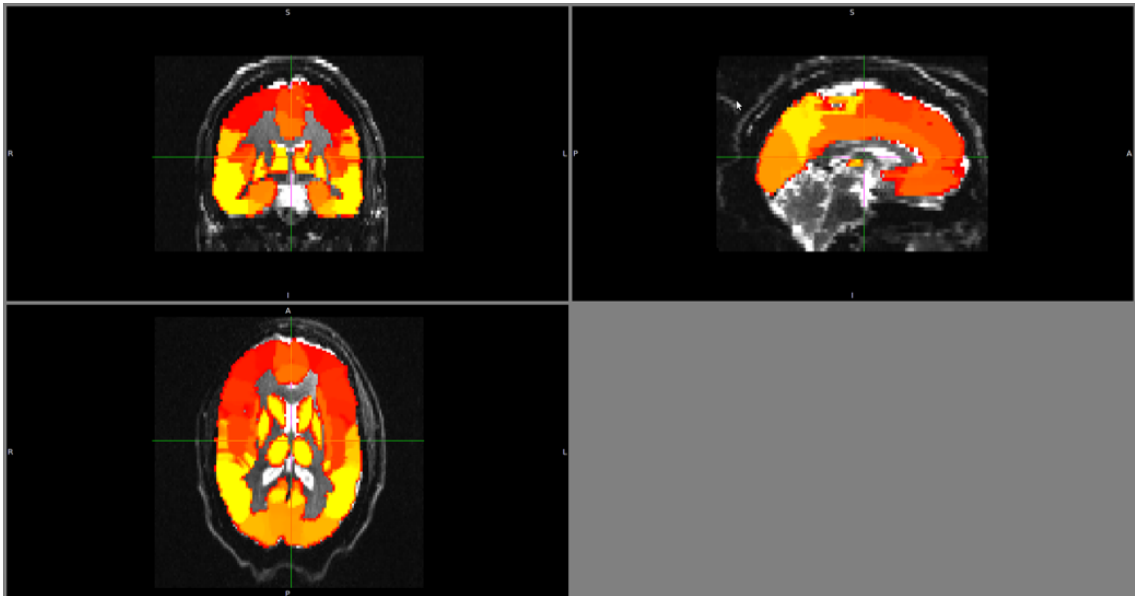


Figure 2.4: Registered grey matter mask example

### 2.4.1 Diffusion Tensor Imaging (DTI) and BEDPOSTX

We mentioned in Section 1.2 that directional magnetic field gradient is applied to water molecules. The modulating effect of the magnetic field weighting at direction  $j$  is reflected by a scalar factor  $b_j$  and a vector  $\mathbf{v}_j$  defining its direction. Here we leave out details about how  $b_j$  is related to the physical attributes, because this doesn't affect the understanding of the model. The DTI imaging model is formulated as [26]:

$$s_j = s_0 \exp(-b_j \mathbf{v}_j' \mathbf{D} \mathbf{v}_j) \quad (2.4)$$

where  $s_j$  is the measured signal,  $s_0$  is the reference signal without diffusion weighting,  $\mathbf{D}$  is a  $3 \times 3$  matrix representing the diffusion tensor. The diffusion tensor represents an ellipsoid in the 3D space, with its eigen vectors serving as the three principal directions. The ellipsoid illustrates the diffusion directions. An isotropic ball indicates that there is unlikely to be a fiber present, while a spiky shuttle implies high probability of a fiber orienting at the corresponding direction.

The actual model used in FSL BEDPOSTX made some modifications to this formula, leaving only one principal direction of the diffusion tensor:

$$s_j = s_0 [(1 - \lambda) \exp(-b_j d) + \lambda \exp(-b_j d (\mathbf{v}_j' \mathbf{x})^2)] \quad (2.5)$$

where  $\lambda$  can be understood as the fraction of the voxel that is anisotropic,  $d$  is the mean diffusivity,  $\mathbf{x}$  is the direction of the anisotropic portion (i.e. the fiber).

The BEDPOSTX tool in FSL models the signal model probabilistically, so that the unknown parameters  $\lambda$ ,  $d$  and  $\mathbf{x}$  are regarded as random variables. Parameter

estimation is formulated as a Bayes inference problem, and Markov Chain Monte Carlo (MCMC) sampling is used to estimate the posterior distribution of the model parameters.

## 2.4.2 Probabilistic Tractography

The FSL tractography tool, `probtrackx`, does probabilistic tractography based on the diffusion parameters estimated by `BEDPOSTX`. Seed voxels or a seed region mask must be specified for `probtrackx`. From each seed voxel a number of streamlines are initiated in both directions. For each voxel reached by the streamline, it is redirected according to the directional probability distribution estimated by `BEDPOSTX`. A streamline is terminated when some directionality measure falls under a certain threshold, or some other constraint is broken. In order to compute the connectivity matrix, one or two target masks must also be specified. If the matrix option is switched on and a target mask is specified, connectivity matrix entries corresponding to all pair of points within the target region on a streamline are updated upon a streamline tracking is completed. Streamlines that do not terminate in the target region for either end will be disregarded.

## 2.5 Specific Processing Pipeline for the Schizophrenia Data

The techniques introduced in Sections 2.3 and 2.4 cover most of the functionalities in FSL that we use to process our data. This section introduces the details about how they are performed.

We performed nonlinear registration between each individual raw DWI image data and the standard MNI152 T1 weighted image, getting both the diffusion-to-standard and the standard-to-diffusion warp field. The standard-to-diffusion warp field is then used to register the JHU white matter atlas and the AAL-90 atlas to each individual diffusion space (the AAL-90 atlas has been pre-processed to fit into the standard space).

On the other hand, BEDPOSTX is performed on each of the individual diffusion image. Probtrackx is then applied to each individual with seed mask specified as the registered JHU white matter atlas (union of all labeled regions), and the target mask specified as the AAL-90 atlas (union of all labeled regions). Probtrackx returns a file recording the coordinates of voxels in the region of interest (ROI, i.e. the region delineated by the target mask). and a file representing the voxel-wise connectivity matrix. There are typically 100,000 to 150,000 voxels in the ROI, so it is in general impossible to store the full connectivity matrix in memory. The connectivity file represents the matrix in a sparse format. Each connectivity file typically has about 100,000,000 to 200,000,000 entries. The reason we use the JHU white matter atlas as the seed region instead of the whole brain is mainly to reduce the computational cost. Since most of the major fiber bundles resides in the white matter region, this does not seriously reduce the precision of the estimation. For the same reason we set the number of sampled streamlines from each seed voxel to a relatively small number, 50, while the default is 5,000. We found that this does not affect the tractography results very much in practice.

The connectivity matrix is then ready to serve as input to the clustering (par-

cellation) algorithm. In the next chapter we will focus on the formulation and solution of the parcellation problem.

## Chapter 3: Parcellation of an Individual Connectivity Matrix

### 3.1 Connectivity Profile and the Graph-Cut Formulation

In the literature, many intuitions have been developed as criteria for deciding whether certain brain voxels should be clustered into the same homogeneous region or not. For example, in fMRI analysis, voxels having strong time-correlated activation can be regarded as belonging to a region or a functional network [14]. In terms of structural networks, connectivity profile is a widely used signature for parcellation studies (e.g. [27–29]). The connectivity profile for a voxel is the set of endpoints connected to this voxel by streamlines and the corresponding connectivity values. It is a reasonable assumption that voxels having similar connectivity profiles also have similar functional roles and thus should be grouped together.

While similarity of connectivity profiles is a good measure of the similarity of structural position of voxels, technical issues need to be addressed: 1) The signature of the connectivity profile, i.e. how should we encode the connectivity profile so that it is both accurate and also not too costly to compute; 2) Spatial placement intuition, i.e. we should also integrate spatial closeness information into clustering to avoid spurious clusters. Voxels far from each other are unlikely to belong to the same parcellation even if they have similar connectivity profiles. This intuition cannot be

reflected by the connectivity matrix data itself.

For the first problem, the most accurate representation of a connectivity profile is a list of coordinates of the connectivity profile. But in this case we have to perform an  $O(n^2)$  matching algorithm (or at best  $O(n \log n)$  if we use a spatial tree index to store the data) before computing the similarity, therefore this is only practical if each connectivity profile only has a very few number of connections. This is not true for probabilistic tractography, where each voxel usually projects streamlines to many ending voxels, although many of them have very small connectivity value. In our framework we construct the connectivity profile by first coarsening the space, grouping the voxels into cells of size  $4 \times 4 \times 4$  voxels, and counting the connectivities to each of these coarsened cells. The problem with this approach is the “cross-cell-boundary artifact”. Since adjacent cells are not distinguished from far-away cells, similar connectivity components that happen to fall into adjacent coarsened cells can lose their similarity information. To alleviate such problem, a Gaussian smoothing is performed after computing the connectivity profile. With Gaussian smoothing the other endpoint of a streamline is modeled as having a 3D Gaussian distribution centered at the actual endpoint. The connectivity profile of a voxel is then understood as the set of its posterior expected connectivity to each of the coarsened cells.

For the second problem, we formulate the parcellation as such a graph cut problem where the topology of the graph has nothing to do with the connectivity data. The topology of the graph is just a grid reflecting the spatial adjacency, termed “spatial graph”. It can simply be a rectangular grid with only adjacent

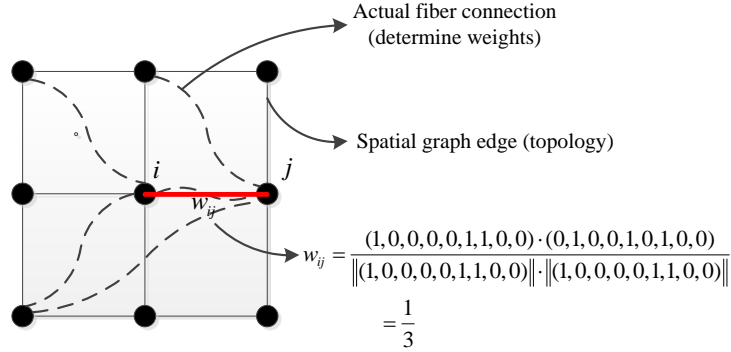


Figure 3.1: Topology and connection weights of the formulated graph-cut problem

voxels connected, or less sparse to include neighbors of voxel that are a few voxels away. The connectivity profile information only contributes in calculating the connection weights of the spatial graph. The connection weights of a link in the spatial graph is a similarity measure of the connectivity profiles of its two endpoints. In the experimental results reported in this thesis, the cosine distance is used as the measure of similarity between two connectivity profile vectors. The graph is represented by a weighted adjacency matrix  $\mathbf{W}$  (stored in a sparse format), termed “similarity matrix” from hereafter. Figure 3.1 illustrates the spatial graph model. The parcellation can then be formulated as the graph cut problem on the spatial graph. The general objective of a multi-class graph cut algorithm is to partition the graph into  $K$  components so that the total weights of the links whose terminals are in different components are minimized.

## 3.2 Algorithms for Solving the Graph Cut Problem

Graph cut problems are generally NP-hard problems. In fact, approximating the solution of a balanced graph cut problem with any finite factor is NP-complete [30]. Yet many heuristic methods have been proposed and have been shown to achieve good performance in practice.

Graph cut algorithms can be categorized into two major types, global methods and local methods. In our project, we use both a global method, the spectral clustering, and an original local method, the “Multi-class Hopfield Network” method.

### 3.2.1 Spectral Clustering

Spectral clustering uses eigen-decomposition of the similarity matrix of a graph to approximate the min-cut solution [31–33]. It has been one of the most popular class of graph partitioning algorithms, with successful applications especially in image segmentation. Spectral clustering starts by constructing the “Laplacian matrix” from the similarity matrix  $W$ :

$$\mathbf{L} = \mathbf{D} - \mathbf{W} \tag{3.1}$$

where  $\mathbf{D}$  is a diagonal matrix with  $\mathbf{D}_{ii} = \sum_j \mathbf{W}_{ij}$ . The Laplacian is normalized for the purpose of balancing the clusters:

$$\mathbf{L}_{norm} = \mathbf{D}^{-\frac{1}{2}} \mathbf{L} \mathbf{D}^{-\frac{1}{2}} \tag{3.2}$$

The following generalized eigen value problem is solved to get the first  $K$  eigen vectors (eigen vectors corresponding to the  $K$  smallest eigen values).

$$\mathbf{L}_{norm} \mathbf{u} = \lambda \mathbf{L}_{norm} \mathbf{D} \mathbf{u} \quad (3.3)$$

The eigen vectors  $\mathbf{u}$  excluding the first one (will be all-one vector in theory and corresponds to the eigenvalue 0) are stacked to a matrix  $\mathbf{U}$  of size  $n \times (k - 1)$  ( $n$  is the number of voxels in ROI). The k-means is then applied to the rows of  $\mathbf{U}$  to get the cluster labels of each voxel.

According to the Rayleigh-Ritz theorem [34], the eigen solution solves the problem

$$\begin{aligned} \min_{\mathbf{H}} Tr(\mathbf{H}' \mathbf{L}_{norm} \mathbf{H}) \\ \text{subject to } \mathbf{H}' \mathbf{D} \mathbf{H} = \mathbf{I} \end{aligned} \quad (3.4)$$

if  $\mathbf{H}$  is constrained as

$$\mathbf{H}_{ij} = \begin{cases} \frac{1}{\sqrt{vol(C_j)}} & \text{if } i \in C_j \\ 0 & \text{otherwise} \end{cases} \quad (3.5)$$

Then the problem is exactly equivalent to solving the normalized min-cut problem desired:

$$\min_{S_1, S_2, \dots, S_K} Ncut(S_1, S_2, \dots, S_K) = \sum_{i=1}^K \frac{cut(S_i, \bar{S}_i)}{vol(S_i)} \quad (3.6)$$

where  $S_i$  denotes the set of nodes within cluster  $i$ ,  $cut(S_i, \bar{S}_i)$  denotes the total weights of the links to be cut to separate  $S_i$  from the rest of the nodes, and  $vol(S_i)$

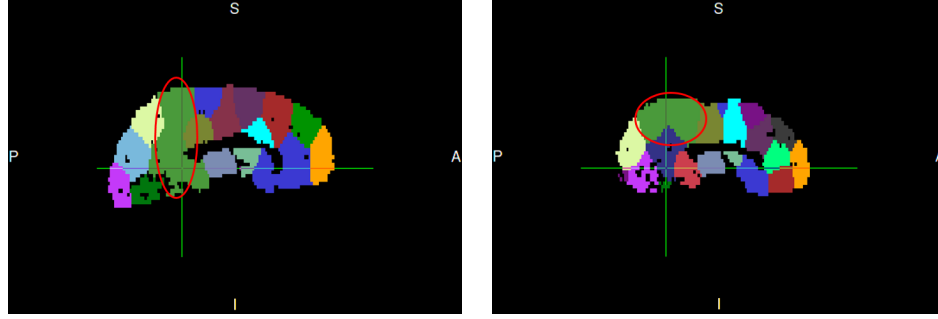
is the number of nodes (volume) of  $S_i$ . The eigen solution is therefore a continuous space approximation of the discrete clustering solution.

To problems where there is high node degree heterogeneity, regularized spectral clustering (RSC, [35,36]) can help improve the performance. In RSC, computation of the normalized Laplacian matrix is varied as

$$\mathbf{L}_{norm,reg} = (\mathbf{D} + \tau\mathbf{I})^{-\frac{1}{2}}\mathbf{L}(\mathbf{D} + \tau\mathbf{I})^{-\frac{1}{2}} \quad (3.7)$$

Spectral clustering performs well with a relatively few number of clusters. The challenge with spectral clustering is that the result is highly dependent on the specific initialization of the centroids in the k-means step. This poses a significant difficulty to preserve consistent region definitions across subjects so that group analysis is possible. Although it is possible to enforce a common initialization to all the subjects in a group, the initialization has such a low degree of freedom (number of clusters desired) that it does not impose sufficient constraints to enforce consistent definition of clustered regions. Figure 3.2 shows the spectral clustering result of two subjects S0370 and S0449, with a common k-means initialization derived from the AAL-90 atlas. We can see that despite the common initialization, many regions, such as the one circled in red, has totally lost its definition in the AAL-90 atlas.

The cross-subjects inconsistency problem can be somewhat alleviated by the local update method introduced in the next section. In that method, initialization can be enforced as the actual cluster labels of each voxel, so that entire parcellation boundaries are confined near the initial region definitions. This makes parcellation



(a) S0370

(b) S0449

Figure 3.2: Spectral clustering will corrupt region definitions across subjects

results of different subjects comparable and thus group analysis is then possible.

### 3.2.2 Multi-class Hopfield Network

To address the cross-subjects inconsistency problem, we propose a special clustering algorithm based on a multi-class version of the Hopfield network model [37], termed the “Multi-class Hopfield Network (MHN)”. The algorithm starts from an initial assignment of cluster labels - instead of the cluster centroids - and gradually evolve to a better parcellation arrangement. Therefore the region definitions provided by the initial assignment can be somehow preserved across different subjects.

Hopfield networks were originally proposed to model associative memory. A standard Hopfield network is formulated by a weighted graph with binary node values (1 or -1). Upon retrieval of stored memory, the update rule attempts to find the local minimum of the energy function (assuming no nodal bias is introduced)

$$E = -\frac{1}{2} \sum_{i \neq j} w_{ij} x_i x_j \quad (3.8)$$

Intuitively the optimal solution will tend to assign opposite labels to terminals of edges of small weights and the same labels to terminals of edges of large weights. Thus it serves as a good criterion function to be minimized in order to find a good graph cut.

The update rule for retrieving a local minimum of the energy is very simple: in each iteration, first select an arbitrary order for node updates, then apply the following update rule according to the selected order.

$$x_i \leftarrow \text{sgn} \left( \sum_j w_{ij} x_j \right) \quad (3.9)$$

It is guaranteed that the update will converge at a local minimum. To generalize the model to deal with multi-class scenarios, we make a little modification to the energy function and the update rule. In our formulation, the signature of a node is changed to a one-out-of-n vector denoting the cluster affiliation:

$$\mathbf{x}_i = (\mathbf{I}\{1 = c\}, \mathbf{I}\{2 = c\}, \dots, \mathbf{I}\{k = c\})' \quad (3.10)$$

The energy function now becomes

$$E = -\frac{1}{2} \sum_{i \neq j} w_{ij} (\mathbf{x}_i \cdot \mathbf{x}_j) \quad (3.11)$$

And the update rule becomes

$$\mathbf{y}_i \leftarrow \sum_j w_{ij} \mathbf{x}_j \quad (3.12)$$

$$\mathbf{x}_i \leftarrow (\mathbf{I}\{y_{i1} = \max(\mathbf{y}_i)\}, \mathbf{I}\{y_{i2} = \max(\mathbf{y}_i)\}, \dots, \mathbf{I}\{y_{iK} = \max(\mathbf{y}_i)\})' \quad (3.13)$$

It's easy to prove that a similar convergence theorem holds for the Multi-class Hopfield Network framework. However, the solution easily falls into a local optimum. To somewhat mitigate the local optimum problem, simulated annealing can be applied to help the search jump out of local minima. The update rule with simulated annealing is

$$\mathbf{z}_i \leftarrow \frac{\exp(\mathbf{y}_i/T^{(t)})}{\sum_{j=1}^K \exp(y_{ij}/T^{(t)})} \quad (3.14)$$

$$\mathbf{x}_i \leftarrow \{\mathbf{e}_k \text{ with probability } z_{ik}\} \quad (3.15)$$

$$T^{(t+1)} \leftarrow \alpha T^{(t)} \quad (3.16)$$

where  $\mathbf{e}_k$  denotes a vector with only one non-zero entry at position  $k$ ,  $T$  specifies the “absolute temperature” for the cool-down process.  $\alpha$  is a factor less than 1 that controls the rate of cooling. Simulated annealing permits certain probability of assigning a cluster label that is not best in the greedy sense, therefore provides chances for jumping out of a local optimum.

We tested the correctness of the algorithm with some randomly generated synthetic graph data. The graphs are generated with preset number of clusters and number of nodes per cluster. Sparse links are generated according to preset linking probabilities for intra-cluster nodes and inter-cluster nodes, respectively. Existing

links are assigned with similarity weights randomly generated with different distributions for intra-cluster and inter-cluster links, respectively. To give a quantitative assessment of different clustering methods, we follow a similar procedure as the Levine and Domanys Resampling Approach [38]. Since we have the ground-truth for our synthesis experiment, we do not really need to do any resampling. For both the ground truth labeling and the labeling obtained by the clustering algorithms, we construct a  $N \times N$  binary matrix ( $N$  is the number of nodes in the graph)  $F$  where each of its binary element  $f_{ij}$  represents whether nodes  $i$  and  $j$  are of the same cluster. The quality of a clustering algorithms is then evaluated using the quantity

$$Q = \frac{\sum_{i,j} \delta \left( f_{ij}^{(truth)}, f_{ij}^{(clustering)} \right)}{N^2} \quad (3.17)$$

Where  $\delta(\cdot, \cdot)$  is the indicator function representing whether its two binary arguments are of the same value.

We evaluated the performances of the Multi-class Hopfield Network, Multi-class Hopfield Network with simulated annealing, spectral clustering, a variation of spectral clustering using raw similarity matrix and largest eigen vectors. The results for different test cases are shown in Figure 3.3. Surprisingly, when equipped with simulated annealing the Hopfield network method performs better than spectral clustering methods. For the Hopfield network without simulated annealing, its error mainly comes from clustering two or more distinct clusters into one grand cluster, therefore the performance index degrades drastically when number of clusters gets large; But it rarely makes cross-cluster mistakes. Note that this synthetic experi-

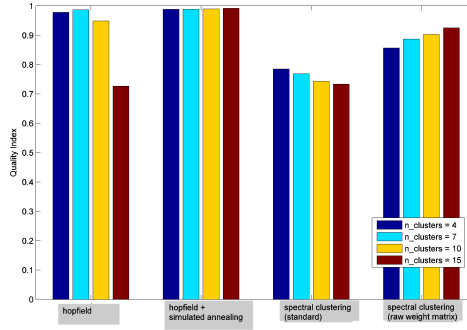


Figure 3.3: Performances of clustering algorithms on the synthetic graph data. Experiment setup: 7 nodes in each clusters, nodes are connected with probability 0.5, intra-class link weights have distribution of  $Gaussian(0.5, 0.5^2)$ , inter-class link weights have distribution of  $Gaussian(-0.5, 0.5^2)$ . Hopfield network with simulated annealing performs best in all cases.

ment only serves to test whether a reasonable solution or not the proposed Multi-class Hopfield Network method is. It should not be regarded as an evidence that MHN performs better than spectral clustering in general. Actually we also tested these algorithms on some simple 2D shape sets including “Aggregation” [39], “Compound” [40], “Pathbased” [41], “Spiral” [41], “D31” [42], “R15” [42], “Jain” [43] and “Flame” [44] (data files are downloaded from <http://cs.joensuu.fi/sipu/datasets/>). On some of these datasets, it is possible to select appropriate graph and distance configurations to make spectral clustering work better than MHN.

## Chapter 4: Individual Subjects Parcellations and Group Analyses

### 4.1 Growing Individual Brain Parcellations

The parcellation of each subject is first initialized by the AAL-90 atlas. Registrations from the MNI space to the subjects' diffusion spaces are first obtained using FNIRT in FSL. The AAL-90 atlas is segregated into 90 binary images and each is transformed to the subjects' diffusion spaces using the registration warp field. The registered regions serve as the starting point of Multi-class Hopfield Network (MHN) updates.

The MHN update rule is then applied to each subject's data with a maximum of 100 iterations. Then label vectors after these iterations are converted back to value indices for visualization and group analyses.

The actual implementation used is the variance of the MHN with simulated annealing, described in (3.14), (3.15). However the initial temperature  $T^{(0)}$  is set very low to prevent the corruption of the initial formulation of the regions.

## 4.2 Group Study of Schizophrenia Patients

Two group studies are performed to show the effectiveness of the proposed parcellation method in clinical research. In the first study we extract individual voxel volumes of each defined region, and connectivity value between each pair of defined regions, and perform two-sample t-test over the schizophrenia vs. the normal group. We detect significantly changed regions/connections. In the second study we use these region volume/connectivity data as features to train linear Support Vector Machine(SVM) classifiers. We compare the classification precisions with those obtained by using the AAL-90 atlas.

## 4.3 Results

### 4.3.1 Visual Scan of Parcellation Results

Parcellation results for two subjects are shown in Figure 4.1: S0229 (a schizophrenic subject) and S0449 (a normal subject). The figure only shows a side view and its purpose is to illustrate some group consistent differences between the AAL-90 atlas and the connectivity based atlas. Two kinds of salient deformations are found to be consistent across most of the subjects and are circled using red and yellow, respectively. Clearly visual inspection is not sufficient to compare subjects in the two groups, but we can get some intuition about significant differences in the red region for example, which are consistent with the t-test results shown later (Region 27, in the red circle which is colored light green, has significant volume change in

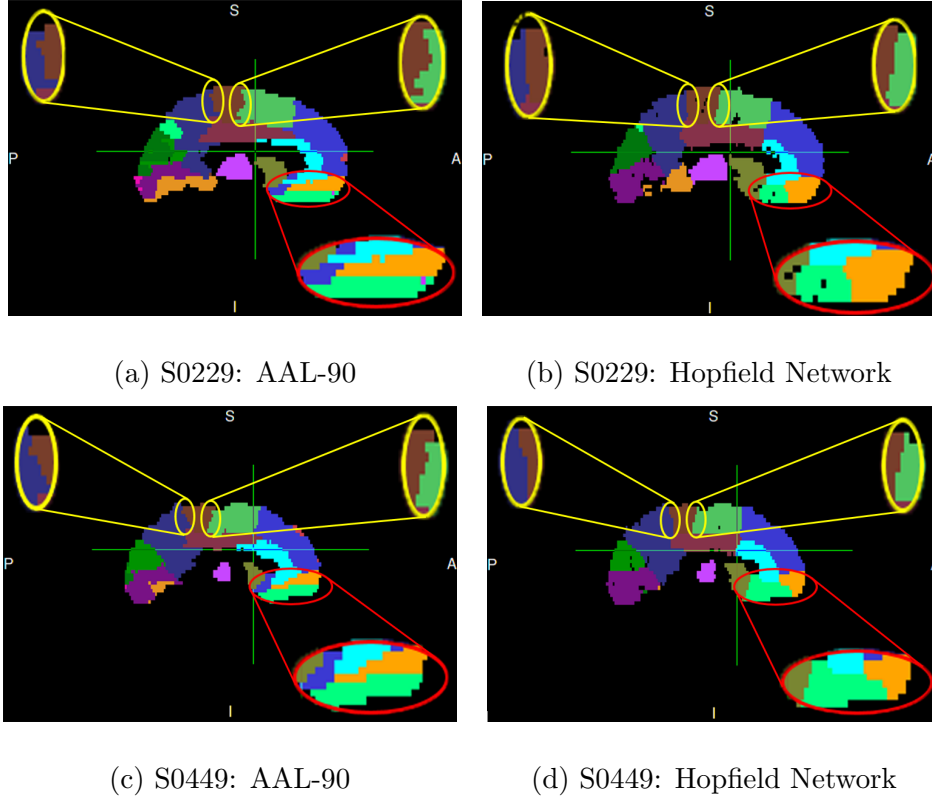


Figure 4.1: Consistent deviations from standard atlas with MHN parcellations

the t-test).

Two group studies were performed to show the effectiveness of the proposed parcellation method in clinical research. In the first study we extract individual voxel volumes of each defined region, and connectivity value between each pair of defined regions, and performed two-sample t-test over the schizophrenia vs. the normal group. This allows us to detect significantly changed regions/connections. In the second study we use these region volume/connectivity data as features to train SVM classifiers. We compare the classification precisions with those obtained from the AAL-90 atlas.

### 4.3.2 Significantly Changed Regions and Connections

To show that the constructed atlas is useful in clinical research, especially in discovering structural causes of the disease, we perform a hypothesis test on whether each of the regions/connections is significantly different between the two groups. In the first experiment, we count the number of voxels of each region in the derived parcellations, and use two-sample t-test to get the p-value that enables us to determine the significance of volume changes between two groups. Since we use pre-defined AAL-90 regions as our initialization and the Hopfield network does not make critical change to these regions, we can name the generated regions with the standard conventions used in the literature and compare our results with previous clinical findings. The regions having the least p-values in the two-sample t-test are shown in Table 4.1. Region volumes are normalized according to individual total brain volumes before computing the p-values. As a baseline for comparison, the volume data acquired from solely AAL-90 atlas registration are also displayed in Table 4.1.

Table 4.1: significant region volume changes detected using the two parcellation methods

<b>Hopfield Network parcellations</b>		<b>AAL-90 parcellations</b>	
Region Name	p-value	Region Name	p-value
82=Temporal_Sup_R	4.61E-06	28=Rectus_R	0.00089239
Continued on next page			

**Table 4.1 – continued from previous page**

<b>Hopfield Network parcellations</b>		<b>AAL-90 parcellations</b>	
Region Name	p-value	Region Name	p-value
30=Insula_R	7.54E-06	27=Rectus_L	0.00155086
27=Rectus_L	0.000105303	31=Cingulum_Ant_L	0.00224055
46=Cuneus_R	0.000128406	63=SupraMarginal_L	0.00397698
86=Temporal_Mid_R	0.000555938	86=Temporal_Mid_R	0.00445966
45=Cuneus_L	0.00196687	89=Temporal_Inf_L	0.0045843
43=Calcarine_L	0.005417029	5=Frontal_Sup_Orb_L	0.00556962
85=Temporal_Mid_L	0.005862056	45=Cuneus_L	0.00591893
57=Postcentral_L	0.005890964	82=Temporal_Sup_R	0.00740954
13=Frontal_Inf_Tri_L	0.007167291	12=Frontal_Inf_Oper_R	0.00763557
59=Parietal_Sup_L	0.012264066	36=Cingulum_Post_R	0.01023098
31=Cingulum_Ant_L	0.013157024	25=Frontal_Mid_Orb_L	0.01218079
28=Rectus_R	0.013672349	87=Temporal_Pole_Mid_L	0.01218086
8=Frontal_Mid_R	0.015191463	32=Cingulum_Ant_R	0.01220685
60=Parietal_Sup_R	0.015690725	46=Cuneus_R	0.01712847
34=Cingulum_Mid_R	0.027025317	81=Temporal_Sup_L	0.02291038
39=ParaHippocampal_L	0.033085883	6=Frontal_Sup_Orb_R	0.02590419
52=Occipital_Mid_R	0.034406422	38=Hippocampus_R	0.03169608
56=Fusiform_R	0.035820728	34=Cingulum_Mid_R	0.03465505

Continued on next page

**Table 4.1 – continued from previous page**

Hopfield Network parcellations		AAL-90 parcellations	
Region Name	p-value	Region Name	p-value
32=Cingulum_Ant_R	0.041195661	26=Frontal_Mid_Orb_R	0.03634662
81=Temporal_Sup_L	0.047860704	85=Temporal_Mid_L	0.03669902
51=Occipital_Mid_L	0.04965823	56=Fusiform_R	0.04687564
16=Frontal_Inf_Orb_R	0.051089719	11=Frontal_Inf_Oper_L	0.04764362

The validity of the two-sample t-test of the region volume analysis hinges on the “regional assumption”, i.e. it builds on the premise that schizophrenia is primarily due to regional volume deficits. Actually the “connectivity assumption” is more prevalent in the schizophrenia research literature, that is, schizophrenia is more related with connection deficits. For the completeness of the work, we also did a significance analysis of the connectivities between the 90 regions. Part of the results are shown in Table 4.2.

Table 4.2: significant region connectivity changes detected using the two parcellation methods

Hopfield Network parcellations			AAL-90 parcellations		
Region 1	Region 2	p-value	Region 1	Region 2	p-value
2=Precentral R	36=Cingulum Post R	7.14E-06	29=Insula L	81=Temporal Sup L	1.26E-06

Continued on next page

Table 4.2 – continued from previous page

Hopfield Network parcellations			AAL-90 parcellations		
Region 1	Region 2	p-value	Region 1	Region 2	p-value
2=Precentral R	35=Cingulum Post L	1.65E-05	26=Frontal Mid Orb R	71=Caudate L	1.56E-06
33=Cingulum Mid L	34=Cingulum Mid R	1.76E-05	25=Frontal Mid Orb L	71=Caudate L	1.23E-05
57=Post- central L	77=Thalamus L	3.58E-05	13=Frontal Inf Tri L	25=Frontal Mid Orb L	1.62E-05
7=Frontal Mid L	13=Frontal Inf Tri L	4.29E-05	19=Supp Motor Area L	59=Parietal Sup L	1.68E-05
46=Cuneus R	68=Precuneus R	0.00010266	57=Post- central L	77=Thalamus L	1.82E-05
34=Cingulum Mid R	73=Putamen L	0.000107775	12=Frontal Inf Oper R	14=Frontal Inf Tri R	2.56E-05
81=Temporal Sup L	85=Temporal Mid L	0.000128248	34=Cingulum Mid R	37=Hippo- campus L	3.36E-05

Continued on next page

**Table 4.2 – continued from previous page**

Hopfield Network parcellations			AAL-90 parcellations		
Region 1	Region 2	p-value	Region 1	Region 2	p-value
19=Supp Motor Area L	36=Cingulum Post R	0.000136104	59=Parietal Sup L	77=Thalamus L	5.01E-05
19=Supp Motor Area L	59=Parietal Sup L	0.000153149	33=Cingulum Mid L	34=Cingulum Mid R	5.41E-05
20=Supp Motor Area R	34=Cingulum Mid R	0.000156602	23=Frontal Sup Medial L	25=Frontal Mid Orb L	6.54E-05
1=Precentral L	78=Thalamus R	0.000207481	17=Rolandic Oper L	81=Temporal Sup L	6.83E-05
23=Frontal Sup Medial L	59=Parietal Sup L	0.000217673	12=Frontal Inf Oper R	52=Occipital Mid R	7.47E-05
13=Frontal Inf Tri L	27=Rectus L	0.00023363	12=Frontal Inf Oper R	18=Rolandic Oper R	0.000100664

Continued on next page

Table 4.2 – continued from previous page

Hopfield Network parcellations			AAL-90 parcellations		
Region 1	Region 2	p-value	Region 1	Region 2	p-value
8=Frontal Mid R	19=Supp Motor Area L	0.000238587	19=Supp Motor Area L	34=Cingulum Mid R	0.000103046
19=Supp Motor Area L	66=Angular R	0.000245982	2=Precentral R	35=Cingulum Post L	0.000110779
27=Rectus L	35=Cingulum Post L	0.000258836	19=Supp Motor Area L	66=Angular R	0.000112625
34=Cingulum Mid R	37=Hippo- campus L	0.000266763	8=Frontal Mid R	12=Frontal Inf Oper R	0.000119972
2=Precentral R	33=Cingulum Mid L	0.000268922	4=Frontal Sup R	71=Caudate L	0.000128102
29=Insula L	81=Temporal Sup L	0.000313395	7=Frontal Mid L	25=Frontal Mid Orb L	0.000129912
30=Insula R	78=Thalamus R	0.000315268	13=Frontal Inf Tri L	85=Temporal Mid L	0.000132738
Continued on next page					

**Table 4.2 – continued from previous page**

Hopfield Network parcellations			AAL-90 parcellations		
Region 1	Region 2	p-value	Region 1	Region 2	p-value
19=Supp Motor Area L	86=Temporal Mid R	0.000326886	23=Frontal Sup Medial L	71=Caudate L	0.00013658
17=Rolandic Oper L	81=Temporal Sup L	0.000392008	31=Cingulum Ant L	34=Cingulum Mid R	0.000136686

### 4.3.3 Classification

In this section we show the results of classifying the normal versus the schizophrenia group using ranked features generated from the proposed parcellations. The classifiers work on many features, thus a combination of possible disease causes can be covered. The disadvantage of such supervised learning analysis is that it does not provide much explanatory information. Yet the classification accuracy provides a strong indication about the quality of our parcellation results.

We perform classification experiments based both on region volume features and connectivity features. The regional volume features and connectivity features are the same quantities that we used to do two-sample t-test in Section 4.3.2. For the regional volume features, both un-normalized and normalized versions are tested.

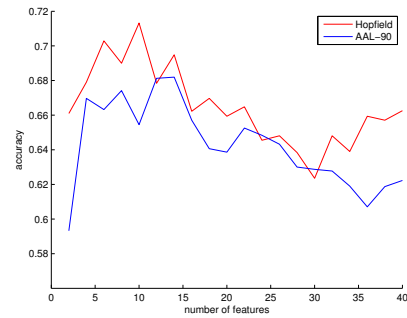
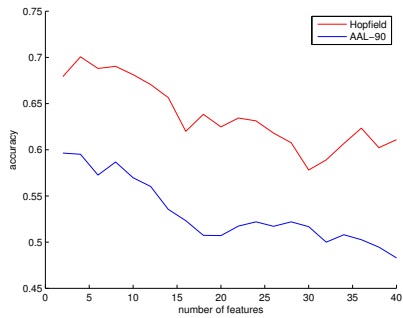
We try different numbers of features, and features are included in order according to their p-value ranks in Table 4.1. In each experiment with a different number of features, we perform 100 trials, and in each trial we randomly sample approximately 3/4 of the whole dataset as the training set (both normal and schizophrenia groups) and use the rest 1/4 as the test set. The mean accuracy result based on 100 trials is recorded for each experiment. Linear SVM is used to build the classifiers (more elaborated classifiers tend to severely overfit).

Figure 4.2 displays the classification results. We can see that the proposed parcellations perform much better than parcellations that are solely based on registered version of the AAL-90 atlas in all three cases.

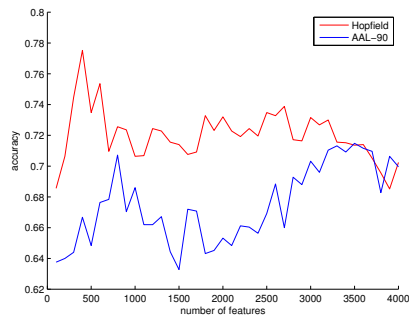
#### 4.4 Discussion of Results

For as many as 90 regions, visual scanning of the parcellation results is not likely to lead to any definite findings, yet we can still find some consistent connectivity parcellation patterns that are different from the AAL-90 atlas in Figure 4.1, including the re-configuration of the regions in the red circle, and the “verticalization” effect in the yellow circles. We can make an interesting assumption that the “verticalization” effect may be due to the gravity during human brain evolution, however whether this is true needs serious and comprehensive verification in the future. For example, it may be just the result of the energy function favoring less edges to be cut off, leading to more regular boundaries.

We perform two-sample t-test on region volumes extracted by our parcella-



(a) Classification Accuracy: Region volume features (un-normalized)      (b) Classification Accuracy: Region volume features (normalized)



(c) Classification Accuracy: Connectivity features

Figure 4.2: Classification performances

tion method and the AAL-90 registration. The top significantly regions detected using the Hopfield network based atlas show lower p-value and higher consistency with some previous clinical results reported in the literature [45], indicating better confidence of the significantly changed regions. However simply looking at the top p-values is not a good way of evaluating the two parcellation schemes, since schizophrenia is a complex disease that may involve many regions, connections and even sub-networks, which cannot be saliently exhibited by the p-values of single regions. More convincing results about the quality of the parcellation is shown in the group classification experiment. The t-test analysis provide a basis of feature selection in the classification experiment.

In the schizophrenia classification experiments, the proposed parcellation scheme excels AAL-90 in all the three feature extraction settings. The most recent schizophrenia research literature favors more the connectivity interpretation to the region volume interpretation. Our results coincide with this trend. Connectivity features extracted using the proposed parcellation scheme perform much better than other schemes, reaching a recognition accuracy of about 78% with 400 connectivity features.

The linear SVM classifier is a black-box prediction system, contributing little to understanding the local structural causes of schizophrenia. The purpose of the classification experiment is only to provide a metric for comparing the quality of the parcellations. The t-test significance is of more interest to clinical research and should be subject to further examination.

## Chapter 5: Group Atlases

### 5.1 Group Atlases Generation

The individual atlases are registered back to the MNI space to perform a simple average to get the (probabilistic) group level atlases. As before, the individual atlases are first segregated into a set of binary images and then registered back one by one. The MNI space atlas of a particular subject is represented by stacking these registered (non-binary) images, with each voxel represented by a 90-dimensional vector. The vector valued atlases from all subjects in the same group are then averaged and normalized to get a probabilistic atlas for the whole group, where the vector for each voxel represents the probability of that the voxel belongs to each of the 90 regions. Voxel-wise group difference is then measured and visualized using a symmetrical metric reflecting the distance between two probability vectors. Since it is hard to perform a hypothesis test on the group difference significance on such high dimensional data, we use an alternative approach: We randomly partition the data into groups with different grouping protocols, and compute a scalar metric indicating total difference between the group atlases for each grouping protocol. Two-sample t-test can then be performed to determine the significance of the “difference of the difference” between a pair of grouping protocols.

The main steps to generate the group level atlases are listed below:

- 1) For each subject, save each of the 90 atlas structures as a binary image.
- 2) Register each of this binary images to the MNI space.
- 3) Combine the 90 binary images for each subject to get an “atlas likelihood vector”, where each of the 90 values of a voxel measures the “likelihood” that this voxel belongs to the specific atlas.

4) Average the atlas likelihood vectors for each group and normalize so that elements of the vector sum to 1, so that we can interpret the vectors as categorical distribution parameters. The group atlas is then constructed by assigning each voxel its most probable cluster label, and colored by the corresponding color of that cluster. We also visualize the voxel-wise “confidence level”, which is simply the likelihood value of the most probable cluster label, so that we can get an intuitive feel about which regions have more consistent connectivity patterns and which regions do not.

5) Compute the difference between the two group atlases. For symmetric and numerical robustness purposes, we use the simple squared Hellinger distance [46] as the measure of difference between two probability vectors . The difference values for each voxel are ordered by magnitude and plotted in a descending order.

6) Measure the significance of several grouping protocols. There were three grouping protocols used: (i) Schizophrenia group vs. normal group (Sch-NonSch); (ii) Randomly selected two groups from the entire dataset (Rand-All); (iii) Randomly selected two groups from the normal subjects (Rand-Normal). For each of the three partitions, we sample 39 subjects in each group for each run, and each

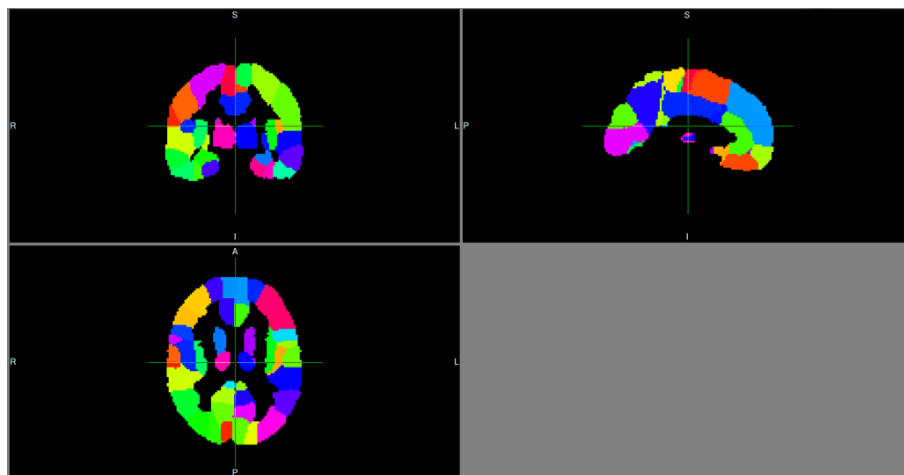
partition is tested for 10 runs. Voxel-wise differences in each run are overlaid and displayed in a single graph.

## 5.2 Results

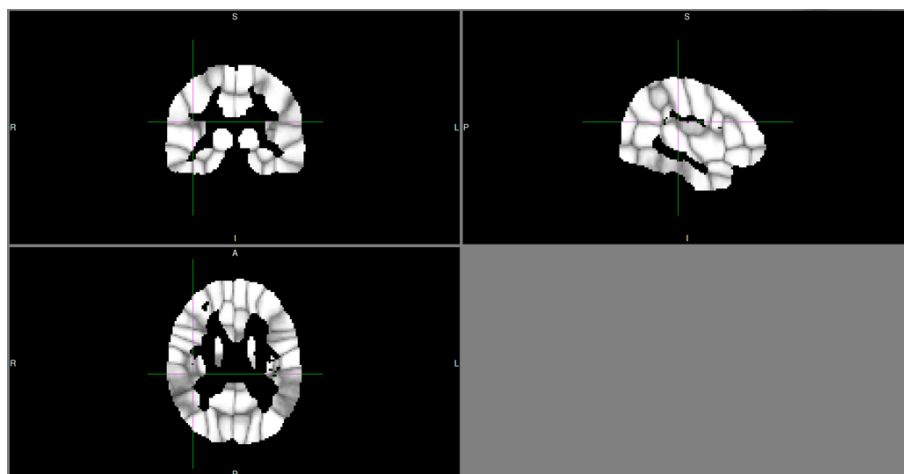
Figure 5.1 shows the atlas for the schizophrenic group and the corresponding confidence level for each voxel. Figure 5.2 shows those for the normal control group. Figure 5.3 displays the voxel-wise difference between the two groups. For example, the cursor is placed as a bright point indicating that the cluster label distribution is significantly different between the two group atlases at that voxel. Further examination will show that this voxel is near the boundary of Region 82, which is the region that showed the most significant volume change according to our two-sample t-test analysis.

Figure 5.4 shows the distribution of voxel-wise differences between several random grouping protocols. The difference values are arranged in descending order of voxel differences.

As described in the previous section, two-sample t-tests are performed to test the significance of “difference of difference” of each grouping protocols. In our experiment 10 random groupings were generated for each random grouping protocol. The p-value for the total differences between Sch-NonSch partition and the Rand-All partition is 0.0016, and the p-value between Sch-NonSch partition and the Rand-Normal partition is 3.3315E-5. This implies that the schizophrenic group has significant systematic atlas structure change against the normal group. This also

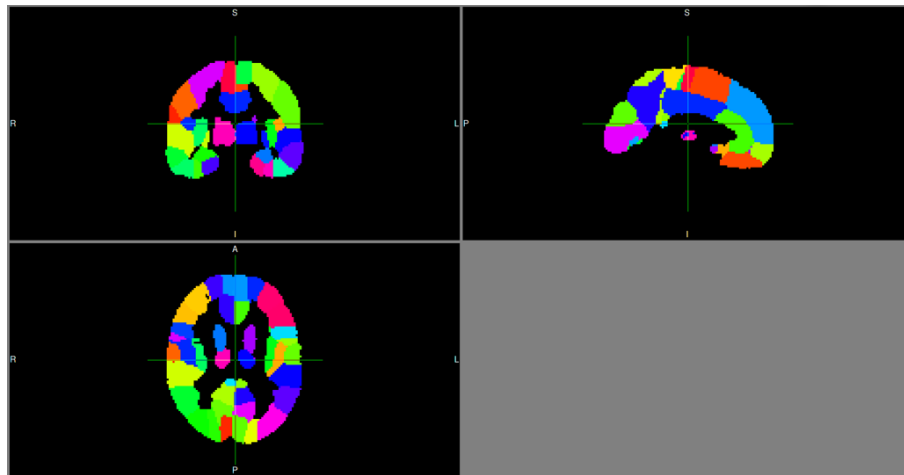


(a) Group Atlas

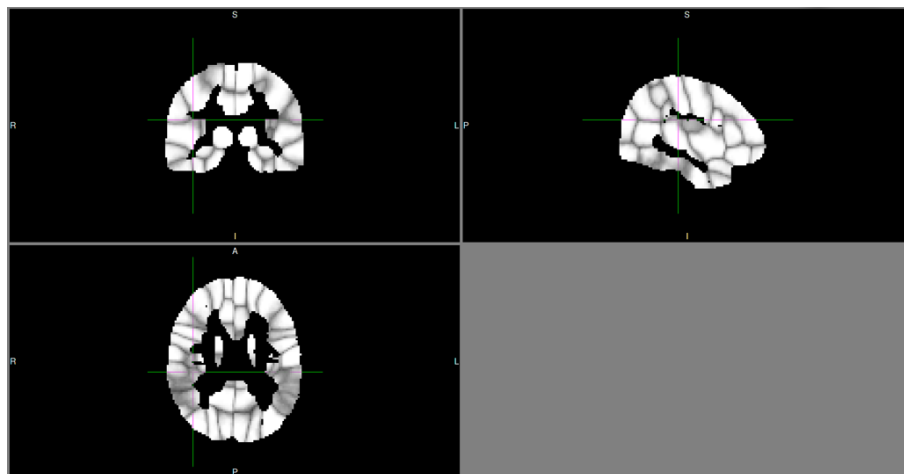


(b) Confidence Map

Figure 5.1: Group atlas of the schizophrenic group



(a) Group Atlas



(b) Confidence Map

Figure 5.2: Group atlas of the control group

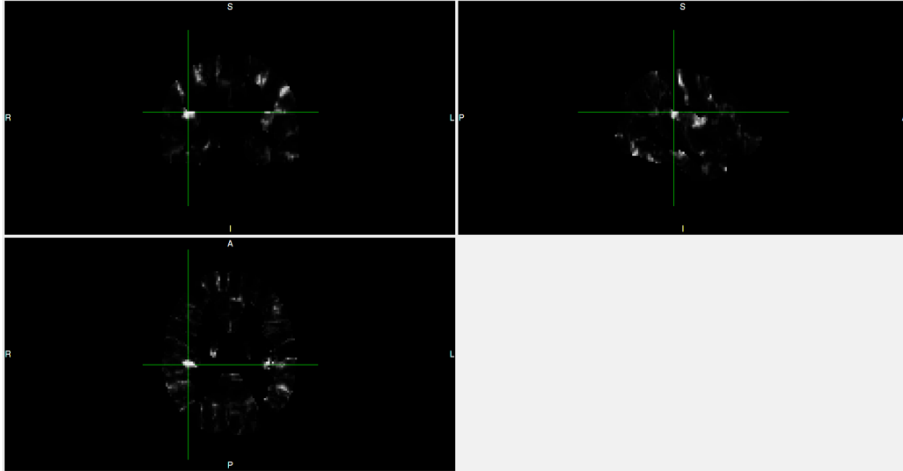


Figure 5.3: Difference map between two group atlases

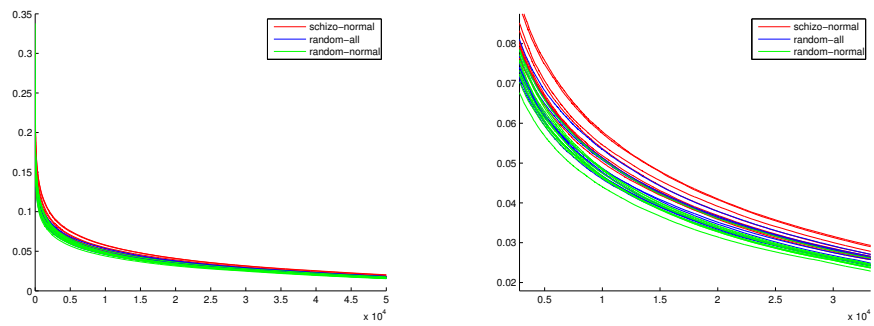


Figure 5.4: Voxel-wise group difference distributions

shows that the schizophrenic group has bigger variance in its connectivity patterns, as compared to the normal control group.

### 5.3 Discussion of Results

We applied a simple registration and averaging scheme to obtain group-level atlases in the MNI space. The averaging removes many of the individual variations and thus results in more regular shapes. The information about individual variations is preserved in the confidence map visualization, from which we can easily tell which regions have more consistent connectivity patterns than others. For example in Figure 5.2b, the regions 81 (left superior temporal), 82 (right superior temporal), 85 (left mid temporal), 86 (right mid temporal) have lower confidence value, indicating lack of consistency of superior/mid temporal regions in terms of their connectivity patterns.

Figure 5.4 indicates that there is a significant amount of group differences between patients and normal subjects that cannot be explained by chance. The two-sample t-test of total difference value further confirms this. The fact that the Sch-NonSch vs. Rand-All displays larger p-value than Sch-NonSch vs. Rand-Normal indicates that a Rand-All group has larger variance than a Rand-Normal group, which in turn indicates that schizophrenia patients have more variance in their connectivity patterns.

There are two major imperfections for the individual parcellation and group analyses framework introduced so far. First, although our method integrates connec-

tivity information into parcellations, it highly relies on initialization of a standard parcellation, and therefore it is not a method to obtain a purely connectivity based atlas. And as is indicated in Fig. 3.2, the AAL-90 atlas does not comply with the connectivity pattern well and therefore may be a bad initialization. To be able to build a connectivity based atlas from scratch (not relying on a pre-defined initialization), we'll need to solve the problem of properly registering the connectivity data to a standard space, so that averaging connectivity data across subjects is possible. Secondly the simple atlas averaging scheme to obtain group-level atlases is not very accurate. The more appealing approach also requires averaging connectivity data directly in a standard space, adding to the importance of work for finding an appropriate way of registering connectivity data. The problem of "registering" the connectivity data to the common MNI space - so that group level averaging can be computed and purely connectivity based atlases can be built from scratch - is addressed in the next chapter.

## Chapter 6: Connectivity Based Atlases Built from Scratch

### 6.1 Overview

The previous described parcellation framework uses the Multi-class Hopfield Network to tune an existing standard atlas to better fit connectivity based analysis. The results highly depend on the standard atlas initialization. This is not quite the ideal framework of our ultimate goal to build a purely connectivity based atlas. As is shown in Figure 3.2, the AAL-90 atlas can be a bad initialization that could be misaligned with the brain connectivity patterns. In this chapter, we aim at building a purely connectivity based atlas, i.e. an atlas that depends solely on connectivity information and does not depend on any kind of initialization with prior knowledge. Separate parcellations for different subjects will not achieve our goal, due to the “cross-subject inconsistency” problem stated in Chapter 3. A feasible solution is to average the connectome data first and then apply clustering on the averaged data. The main challenge is that all subjects in our dataset are in unregistered local diffusion space, and tractography can only be applied in the diffusion space. In the literature, there is no robust way of “registering” the tractography data to the standard space - especially when using probabilistic tractography - where subjects are aligned and averaging is possible. In this chapter, we propose a workflow that

maps the connectivity profiles from the diffusion space to the standard space. A graph cut problem can then be formulated and parcellations are formed from the averaged data in the standard space.

## 6.2 Computing the Connectivity Profiles in MNI Space from Data in Diffusion Space

As we have described in Chapter 3, the connectivity profile for a voxel is defined as a vector of its connectivity numbers to coarsened cells in the full space. The cell size is usually selected much larger than the voxel size, and Gaussian smoothing can be applied to the results to mitigate the “cross-cell-boundary artifact” problem. With 100,000-150,000 voxels in the subjects’ ROIs and the coarsened cell size as  $4 \times 4 \times 4$  voxels, the vector length of a connectivity profile is about 2,000-3,000. In general, it is impossible to store the full connectivity matrix in memory, but it is possible to store the connectivity profiles.

Transformation of the connectivity data between spaces hinges on the coordinate mapping. FSL provides a utility tool that computes the coordinate mapping, but it is very slow (it is a C++ program that read in and process each input coordinate one by one, and hence it is even much slower than a MATLAB implementation that takes advantage of array operations). However we can use the warp field to customize the coordinate mapping code. To do this we first need to convert the default FSL registration output (“warp coefficient”) into warp field format. There is utility tool in FSL that does exactly the transformation from the coefficients to

warp fields. Transformed coordinates for any set of nodes of our choice can then be easily computed by simply subtracting the warp field from the source coordinates.

The coordinate mapping between the diffusion space and the standard space gives us a set of real-value coordinate values. The challenge now is to find a proper way of rounding these values and adjust the corresponding connectivity values. It's not computationally feasible to get a connectivity matrix in the target space, since 1) the full connectivity matrix (non-sparse version) may not fit into memory; 2) if we choose the sparse version, then for each pair of voxels we have to search through all pairs to see if there is a coincident, with a total complexity of  $O(n^2)$  ( $n$  is the number of non-zero entries in the original connectivity matrix, which is of a much larger order of value than total number of voxels, typically over 100,000,000). There is actually also another problem of "resolution holes", which will be described later in this chapter. Instead of trying to migrate the connectivity matrix to the target space, we only compute the connectivity profiles in the target space.

The connectivity profile data has a nice key-value structure: The key is the coordinate of a voxel, the value is the connectivity profile vector associated with that coordinate. With the registration warp field from the diffusion space to the standard space, we propose two efficient solutions of computing the connectivity profile in the standard space: The hash-table solution and the Hadoop solution.

- 1) The hash table solution:

Initialize the diffusion profile hash table, with the key being the diffusion space coordinates and the value being the corresponding connectivity profile vector (defined w.r.t standard space cells), denoted as *profile\_hash* ;

**for** *Each subject in group* **do**

**for** *Each entry in the (sparse) connectivity matrix*

$\{(x_{1,diff}, y_{1,diff}, z_{1,diff}), (x_{2,diff}, y_{2,diff}, z_{2,diff}), l\}$  **do**

            Transform  $(x_{1,diff}, y_{1,diff}, z_{1,diff})$  and  $(x_{2,diff}, y_{2,diff}, z_{2,diff})$  into standard space coordinates  $(x_{1,std}, y_{1,std}, z_{1,std})$ ,  $(x_{2,std}, y_{2,std}, z_{2,std})$ , respectively ;

            Round  $(x_{1,std}, y_{1,std}, z_{1,std})$  and  $(x_{2,std}, y_{2,std}, z_{2,std})$  to their integer-value neighbors. Denote the sets of neighbor coordinates as

$\{(x_{1,std}^{(i)}, y_{1,std}^{(i)}, z_{1,std}^{(i)})\}$  and  $(x_{2,std}^{(j)}, y_{2,std}^{(j)}, z_{2,std}^{(j)})$ , respectively ;

            Compute the distribution factor for each neighbor coordinate according to their distances to the corresponding central coordinate, denoted as  $p_i$  and  $p_j$ , respectively ;

            Look up the cell index corresponding to  $(x_{1,std}, y_{1,std}, z_{1,std})$  and  $(x_{2,std}, y_{2,std}, z_{2,std})$ , denoted as  $k_1$  and  $k_2$ , respectively ;

            Update the corresponding entries in *profile\_hash*:

$profile\_hash[(x_{1,std}^{(i)}, y_{1,std}^{(i)}, z_{1,std}^{(i)})][k_2] =$   
                 $profile\_hash[(x_{1,std}^{(i)}, y_{1,std}^{(i)}, z_{1,std}^{(i)})][k_2] + p_i l,$   
                 $profile\_hash[(x_{2,std}^{(j)}, y_{2,std}^{(j)}, z_{2,std}^{(j)})][k_1] =$   
                 $profile\_hash[(x_{2,std}^{(j)}, y_{2,std}^{(j)}, z_{2,std}^{(j)})][k_1] + p_j l ;$

**end**

**end**

Write *profile\_hash* to disk ;

2) The Hadoop solution:

```
Mapper:      for Each subject in group (that the mapper receives) do
              |
              | Initialize profile_hash as in the hash table solution ;
              | Update profile_hash as in the hash table solution ;
              |
              | for Each (key, value) in profile_hash do
              |   |
              |   | Emit (key, value);
              |   |
              |   end
              | end
              end

Reducer:     for Each key received do
              |
              | Add up the profile vectors corresponding to the key and emit;
              |
              end
```

The hash table solution performs all computations in memory and requires a large memory. The Hadoop solution can take advantage of computation clusters and is more scalable. Luckily we found the hash table solution already meets our time and memory constraints.

After the transformation we obtain connectivity profiles in the standard space, which can then be easily averaged.

We found that there is an implicit problem with the above approach. When we test our scheme on a single subject, we find that the result of spectral clustering is very cluttered, as shown in Figure 6.1. We name this as the “resolution holes” problem. The problem is mostly due to the resolution gap between two spaces. Since each diffusion space voxel is mapped to a single target space voxel, if the target space is higher in resolution compared with the diffusion space, the target voxels will be

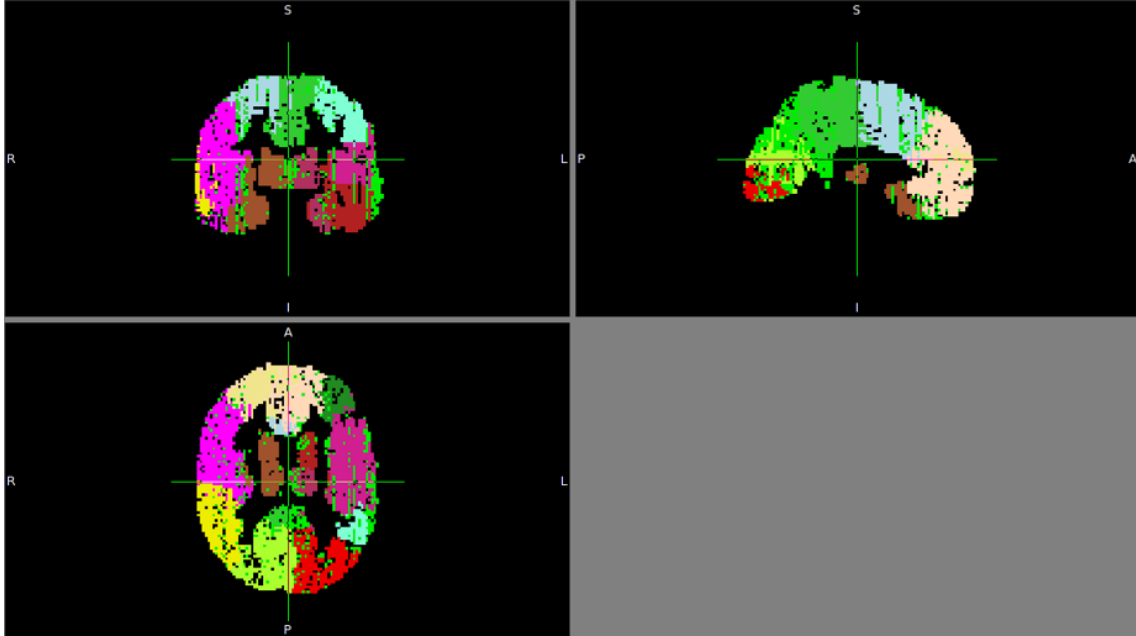


Figure 6.1: Parcellation result with diffusion-to-standard coordinate mapping incurs “resolution holes” problem

sparsely scattered across the space, with many “mishits” that have zero connectivity profile. Since spectral clustering relies heavily on local similarity structures, these missed voxels can be a major hazard to the performance of spectral clustering. Even if the target space has a lower resolution, mishits can still be frequent due to the uneven distribution of displacement vectors of the warp field, as is illustrated in Figure 6.2.

The solution is to use instead the other direction of coordinate mapping, i.e. from the standard space to the diffusion space, as is shown in Figure 6.3. We predefine the set of ROI voxels in the standard space (common to all subjects), and map each of them to a diffusion space coordinate, do proper rounding and averaging to get the final connectivity profile of the target voxel. Since every voxel defined

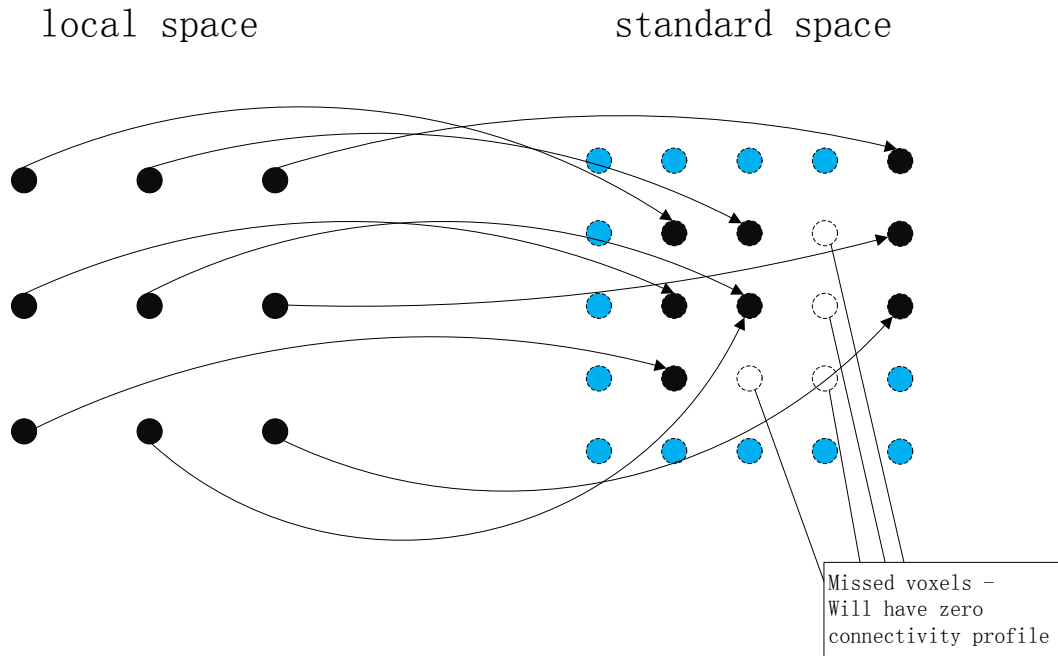


Figure 6.2: “Resolution holes” problem is due to resolution gap and unevenness in the standard space will have its counterparts in the diffusion space (except for voxels at the boundary of the brain), resolution holes will no longer appear. A catch is that although this coordinate mapping is from standard space to diffusion space, we need the elements of a connectivity profile vector to be defined in that standard space to make it possible for integrating across subjects. Therefore we still need the diffusion-to-standard space registration warp field also. The pseudo code for generating the standard space connectivity profile data is summarized in Algorithm 1 and Algorithm 2.

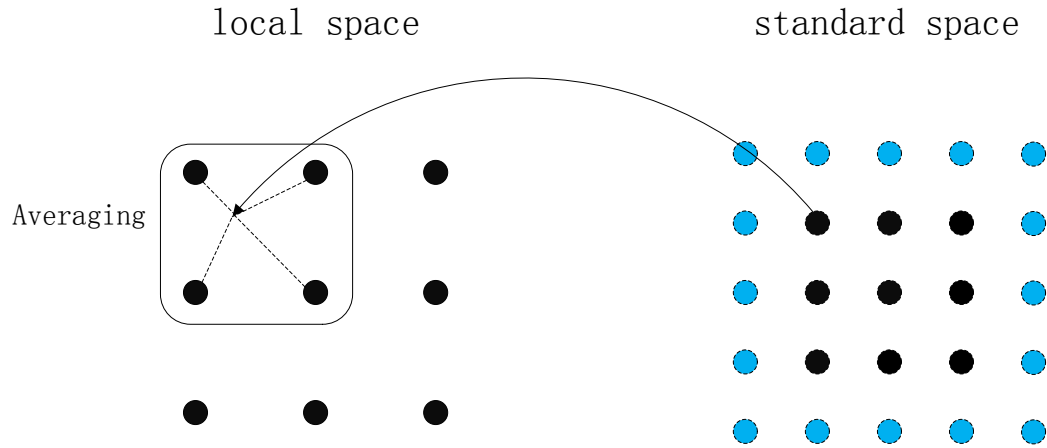


Figure 6.3: Changing the registration to standard-to-diffusion to avoid resolution holes

**Function**  $StandardProfile = GetStandardProfile()$

Initialize the standard space profile hash table, with the key being the standard space coordinates and the value being the corresponding connectivity profile vector (defined w.r.t standard space cells), denoted as  $profile\_hash$  ;

Assign  $DiffusionProfile = GetDiffusionProfileInStandardCell()$  ;

**for** each voxel in standard space ROI **do**

    Transform its coordinate  $(x_{std}, y_{std}, z_{std})$  into the diffusion space, denoted as  $(x_{diff}, y_{diff}, z_{diff})$  (using  $warp\_standard\_to\_diffusion$ ); Round  $(x_{diff}, y_{diff}, z_{diff})$  to find its integer-value neighbors ;

    Assign the connectivity profile vector  $profile\_hash[(x_{std}, y_{std}, z_{std})]$  as the average of those of the integer-value neighbors of  $(x_{diff}, y_{diff}, z_{diff})$  ;

**end**

**Return**  $StandardProfile = profile\_hash$  ;

**Algorithm 1:** Obtaining standard space connectivity profile from (sparse) connectivity matrix in the diffusion space

**Function** *DiffusionProfile = GetDiffusionProfileInStandardCell()*

Initialize the diffusion profile hash table, with the key being the diffusion space coordinates and the value being the corresponding connectivity profile vector (defined w.r.t standard space cells), denoted as *profile\_hash* ;

**for** *each entry in the (sparse) connectivity matrix*

$\{(x_{1,diff}, y_{1,diff}, z_{1,diff}), (x_{2,diff}, y_{2,diff}, z_{2,diff}), l\}$  **do**

Transform  $(x_{1,diff}, y_{1,diff}, z_{1,diff})$  and  $(x_{2,diff}, y_{2,diff}, z_{2,diff})$  into standard space coordinates  $(x_{1,std}, y_{1,std}, z_{1,std})$ ,  $(x_{2,std}, y_{2,std}, z_{2,std})$ , respectively ;

Look up the cell index corresponding to  $(x_{1,std}, y_{1,std}, z_{1,std})$  and  $(x_{2,std}, y_{2,std}, z_{2,std})$ , denoted as  $k_1$  and  $k_2$  ;

Update the corresponding entries in *profile\_hash*:

$$profile\_hash[(x_{1,diff}, y_{1,diff}, z_{1,diff})][k_2] =$$

$$profile\_hash[(x_{1,diff}, y_{1,diff}, z_{1,diff})][k_2] + l,$$

$$profile\_hash[(x_{2,diff}, y_{2,diff}, z_{2,diff})][k_1] =$$

$$profile\_hash[(x_{2,diff}, y_{2,diff}, z_{2,diff})][k_1] + l ;$$

**end**

**Return** *DiffusionProfile = profile\_hash* ;

**Algorithm 2:** Obtaining diffusion space connectivity profile with cells defined in the standard space

A side benefit of this reverse registration procedure is that connectivity profiles for all subjects will be defined on the same set of voxels, thus combining them is a simple matter of averaging the matrices. No further hash table structure is needed in the combining stage (it is needed in the diffusion-to-standard registration approach, since the standard space voxel sets will be different across subjects).

### 6.3 Clustering

Spectral clustering is used to obtain parcellations on the averaged connectivity profile data. Since we aim at obtaining a standard atlas for more general applications in clinical research, we include only the normal subjects in averaging the connectivity profiles. Before doing the clustering we delete the nodes with small connectivity profiles as they mess up with the similarity matrix and dramatically affect the performance of clustering. We set the number of clusters ranging from 5 to 30. This is one of the drawbacks of the spectral clustering - number of clusters has to be pre-defined. For all experiment instances, centroids of the kmeans step are initialized randomly.

### 6.4 Results and Discussion

Figure 6.4-6.9 shows part of the results of clustering on the spatial graph derived from averaged connectivity profiles. We can see clearly that for all cases nice symmetric results are generated even when the initialization is random and no prior symmetrical information is enforced, implying good quality of the clustering results. Some nice hierarchical parcellation structures can be observed as the number of clusters increases. These results show that connectivity profile is a pretty robust criterion for parcellation and atlas generation.

Note that although the results look good, spectral clustering still suffers from sensitivity to initialization. For example the region circled in red in the 25 clusters

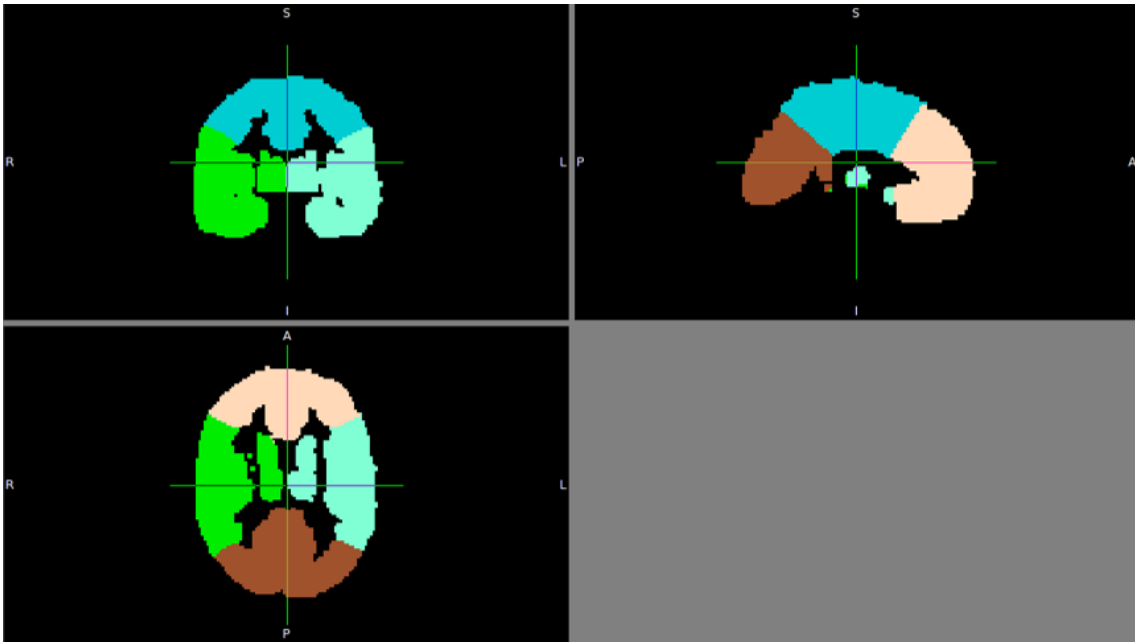


Figure 6.4: Pure connectivity based atlas: 5 clusters

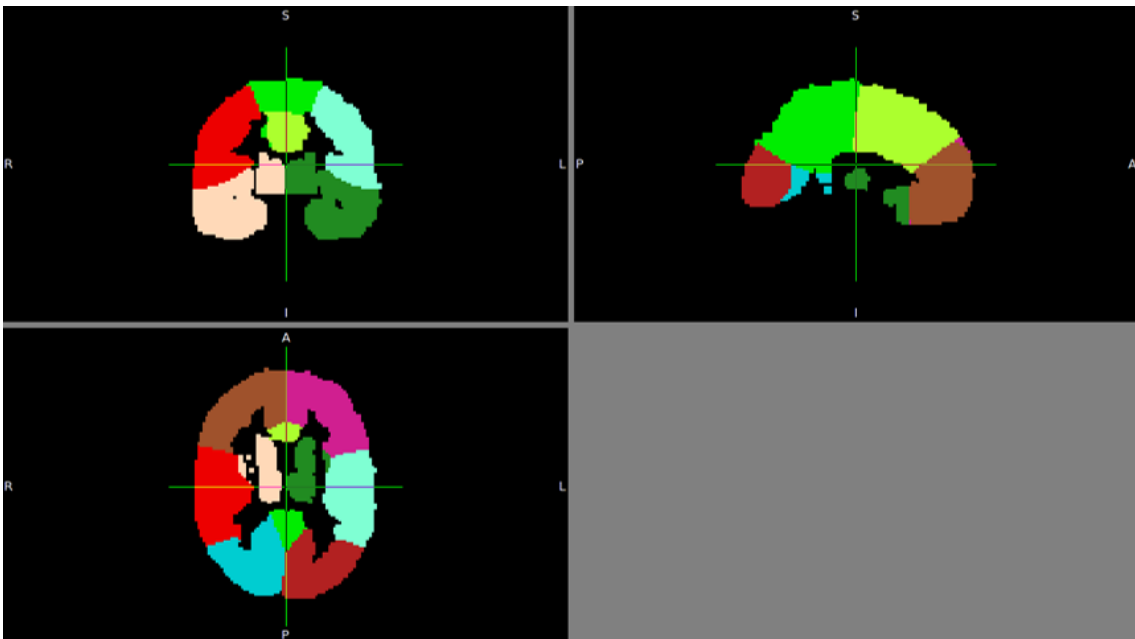


Figure 6.5: Pure connectivity based atlas: 10 clusters

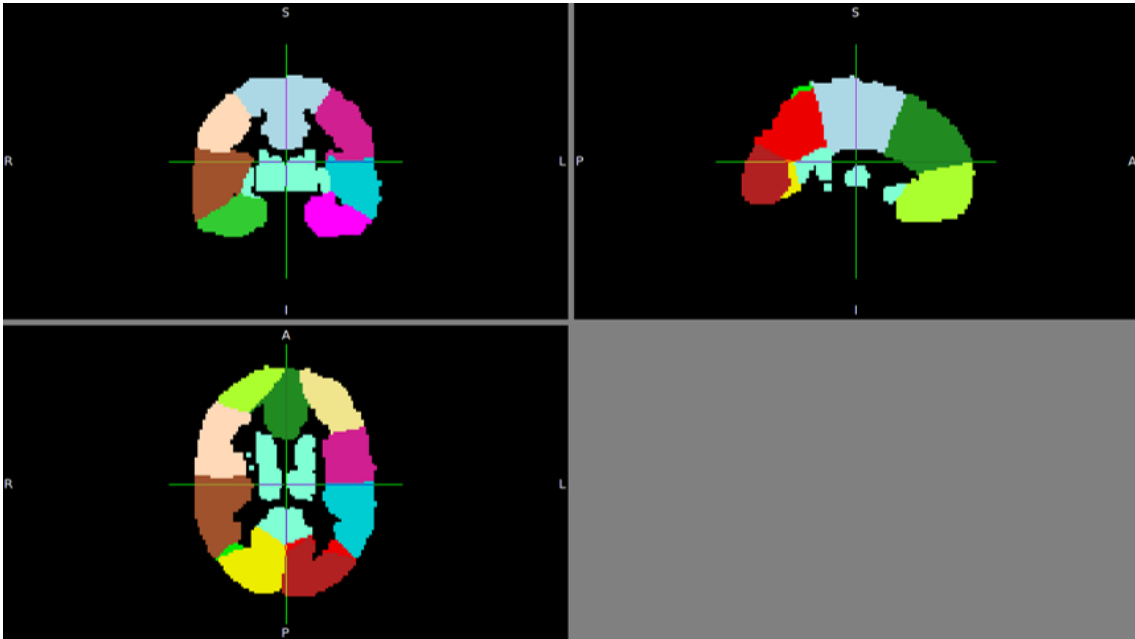


Figure 6.6: Pure connectivity based atlas: 15 clusters

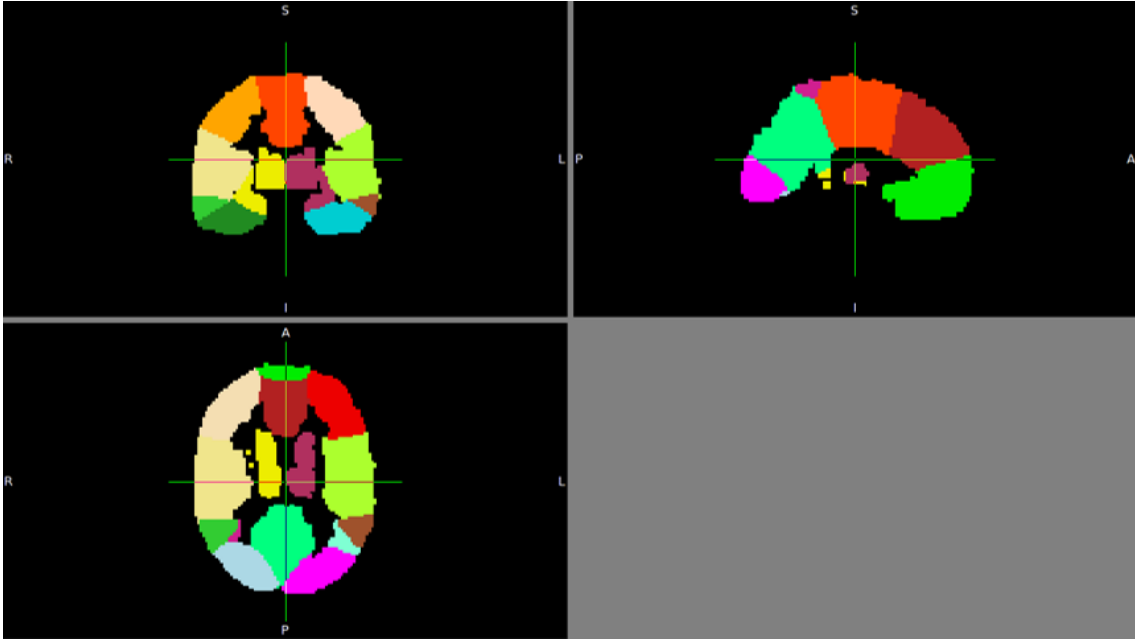


Figure 6.7: Pure connectivity based atlas: 20 clusters

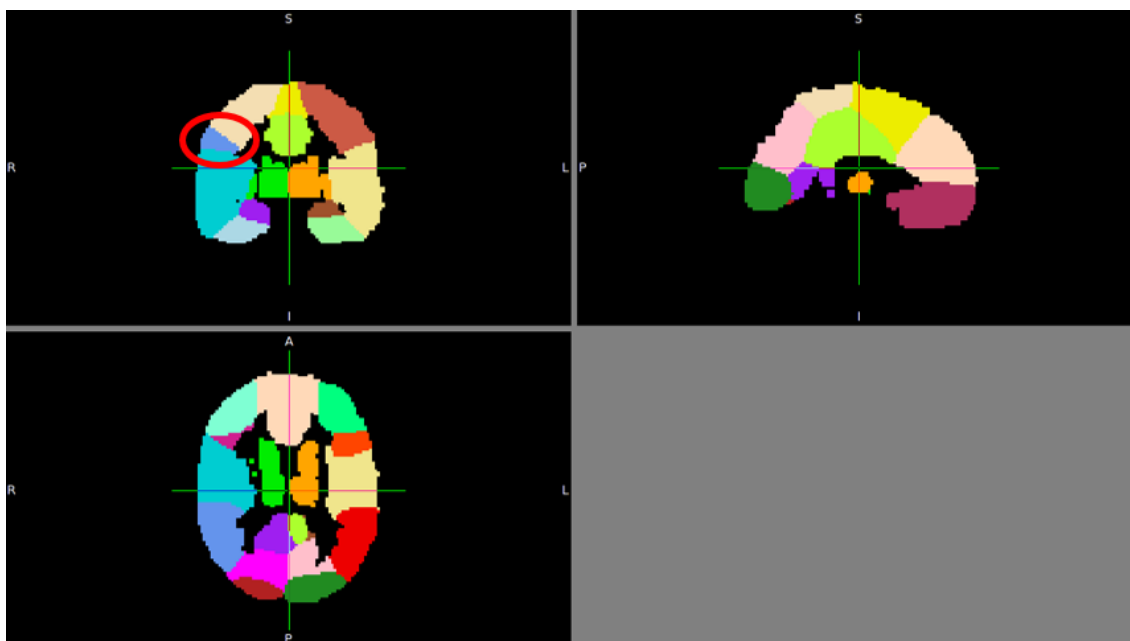


Figure 6.8: Pure connectivity based atlas: 25 clusters

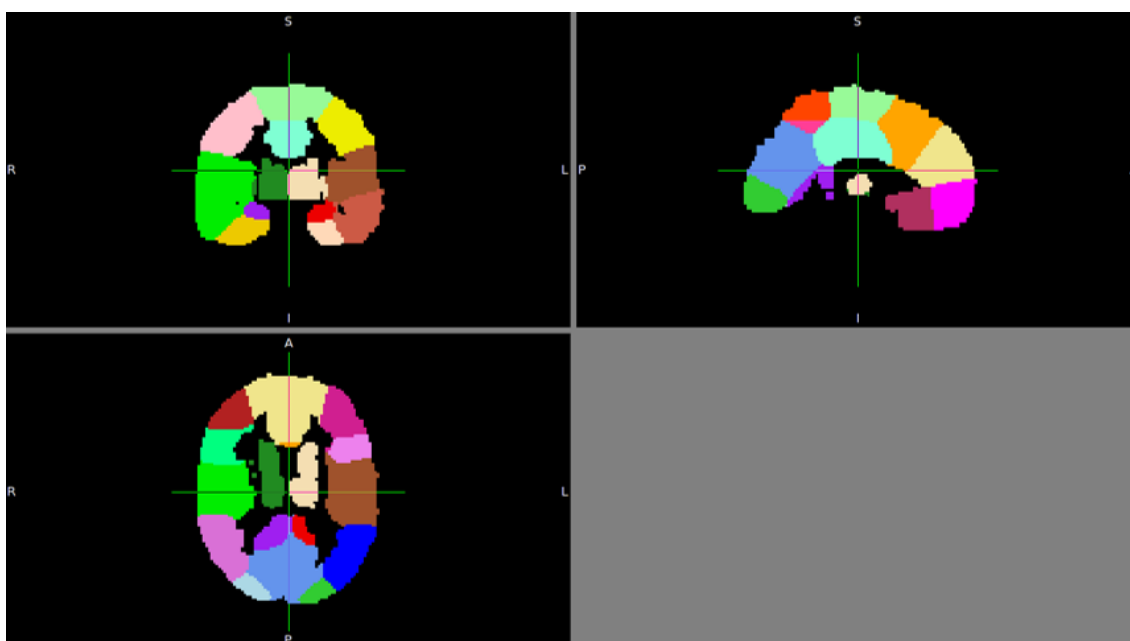


Figure 6.9: Pure connectivity based atlas: 30 clusters

result is likely to be a spurious cluster due to wrong initialization. To really produce a golden standard connectivity based atlas, proper human intervention seems to be inevitable.

## Chapter 7: Concluding Remarks

We propose a connectivity based brain parcellation scheme based on graph partitioning algorithms. The data we work on is the DWI images of schizophrenia and normal subjects, and our main goal is to use the parcellation method to generate discriminating features to separate the two groups of data.

The parcellation method formulates the problem as a graph cut problem where the graph topology is defined by the spatial closeness, and the weights on the graph are defined by similarity of connectivity profiles. Spectral clustering and a proposed Multi-class Hopfield Network (MHN) algorithm are used to solve the graph partitioning. The method can help detect significant regions and connections related with schizophrenia. In building the classifier for separation of the two groups of data, the regional and connectivity features extracted using the proposed MHN method outperform those generated using registered AAL-90 atlas. We also propose a simple scheme of averaging the individual parcellations to form group level atlases for other clinical researches. The schizophrenia group atlas is consistently different from an atlas generated using all data, further verifying the effectiveness of the proposed parcellation method.

To insulate the atlas generation from high dependency to standard atlas initial-

ization and come up with a purely connectivity based atlas, we develop a framework that efficiently aggregate the connectivity information of individual subjects to an averaged connectivity profile in the standard space using hash table. Spectral clustering with random initialization is then performed on the averaged connectivity matrix and show high level of consistency with intuition.

There are still some imperfections in current work. Quantitative and clinical expert verification of the generated atlases are needed. Although the connectivity based atlases shown consistency with intuition, spurious parcellations can still appear due to bad initialization. To build a more reliable brain atlas, human intervention will be indispensable. The future extension of this project will be to build a software interface to let neural scientists interact with the automatic parcellation generation algorithms conveniently to produce semi-automatic parcellations.

## Bibliography

- [1] Ed Bullmore and Olaf Sporns. The economy of brain network organization. *Nature Reviews Neuroscience*, 13(5):336–349, 2012.
- [2] Patric Hagmann, Maciej Kurant, Xavier Gigandet, Patrick Thiran, Van J Wedeen, Reto Meuli, and Jean-Philippe Thiran. Mapping human whole-brain structural networks with diffusion mri. *PloS one*, 2(7):e597, 2007.
- [3] Lav R Varshney, Beth L Chen, Eric Paniagua, David H Hall, and Dmitri B Chklovskii. Structural properties of the caenorhabditis elegans neuronal network. *PLoS computational biology*, 7(2):e1001066, 2011.
- [4] Ed Bullmore and Olaf Sporns. Complex brain networks: graph theoretical analysis of structural and functional systems. *Nature Reviews Neuroscience*, 10(3):186–198, 2009.
- [5] Martijn P van den Heuvel, Rene CW Mandl, Rene S Kahn, Hulshoff Pol, and E Hilleke. Functionally linked resting-state networks reflect the underlying structural connectivity architecture of the human brain. *Human brain mapping*, 30(10):3127–3141, 2009.
- [6] Kaustubh Supekar, Vinod Menon, Daniel Rubin, Mark Musen, and Michael D Greicius. Network analysis of intrinsic functional brain connectivity in alzheimer’s disease. *PLoS computational biology*, 4(6):e1000100, 2008.
- [7] Matthew K Belmonte, Greg Allen, Andrea Beckel-Mitchener, Lisa M Boulanger, Ruth A Carper, and Sara J Webb. Autism and abnormal development of brain connectivity. *The Journal of Neuroscience*, 24(42):9228–9231, 2004.
- [8] Nathalie Tzourio-Mazoyer, Brigitte Landeau, Dimitri Papathanassiou, Fabrice Crivello, Olivier Etard, Nicolas Delcroix, Bernard Mazoyer, and Marc Joliot. Automated anatomical labeling of activations in spm using a macroscopic anatomical parcellation of the mni mri single-subject brain. *Neuroimage*, 15(1):273–289, 2002.

- [9] Katrin Amunts, O Kedo, M Kindler, P Pieperhoff, H Mohlberg, NJ Shah, U Habel, F Schneider, and K Zilles. Cytoarchitectonic mapping of the human amygdala, hippocampal region and entorhinal cortex: intersubject variability and probability maps. *Anatomy and embryology*, 210(5-6):343–352, 2005.
- [10] D Louis Collins, Colin J Holmes, Terrence M Peters, and Alan C Evans. Automatic 3-d model-based neuroanatomical segmentation. *Human brain mapping*, 3(3):190–208, 1995.
- [11] Andrew Zalesky, Alex Fornito, Ian H Harding, Luca Cocchi, Murat Yücel, Christos Pantelis, and Edward T Bullmore. Whole-brain anatomical networks: does the choice of nodes matter? *Neuroimage*, 50(3):970–983, 2010.
- [12] Satoru Hayasaka and Paul J Laurienti. Comparison of characteristics between region-and voxel-based network analyses in resting-state fmri data. *Neuroimage*, 50(2):499–508, 2010.
- [13] Christian F Beckmann, Marilena DeLuca, Joseph T Devlin, and Stephen M Smith. Investigations into resting-state connectivity using independent component analysis. *Philosophical Transactions of the Royal Society B: Biological Sciences*, 360(1457):1001–1013, 2005.
- [14] Yufeng Zang, Tianzi Jiang, Yingli Lu, Yong He, and Lixia Tian. Regional homogeneity approach to fmri data analysis. *Neuroimage*, 22(1):394–400, 2004.
- [15] Pauline Roca, Denis Rivière, Pamela Guevara, Cyril Poupon, and Jean-François Mangin. Tractography-based parcellation of the cortex using a spatially-informed dimension reduction of the connectivity matrix. In *Medical Image Computing and Computer-Assisted Intervention–MICCAI 2009*, pages 935–942. Springer, 2009.
- [16] Pauline Roca, Alan Tucholka, Denis Rivière, Pamela Guevara, Cyril Poupon, and Jean-François Mangin. Inter-subject connectivity-based parcellation of a patch of cerebral cortex. In *Medical Image Computing and Computer-Assisted Intervention–MICCAI 2010*, pages 347–354. Springer, 2010.
- [17] Denis Le Bihan, E Breton, et al. Imagerie de diffusion in-vivo par résonance magnétique nucléaire. *Comptes-Rendus de l’Académie des Sciences*, 93(5):27–34, 1985.
- [18] Klaus-Dietmar Merboldt, Wolfgang Hanicke, and Jens Frahm. Self-diffusion nmr imaging using stimulated echoes. *Journal of Magnetic Resonance (1969)*, 64(3):479–486, 1985.
- [19] DG Taylor and MC Bushell. The spatial mapping of translational diffusion coefficients by the nmr imaging technique. *Physics in Medicine and Biology*, 30(4):345, 1985.

- [20] Mark Jenkinson, Christian F Beckmann, Timothy EJ Behrens, Mark W Woolrich, and Stephen M Smith. Fsl. *Neuroimage*, 62(2):782–790, 2012.
- [21] TEJ Behrens, H Johansen Berg, Saad Jbabdi, MFS Rushworth, and MW Woolrich. Probabilistic diffusion tractography with multiple fibre orientations: What can we gain? *Neuroimage*, 34(1):144–155, 2007.
- [22] Nikos Makris, Jill M Goldstein, David Kennedy, Steven M Hodge, Verne S Caviness, Stephen V Faraone, Ming T Tsuang, and Larry J Seidman. Decreased volume of left and total anterior insular lobule in schizophrenia. *Schizophrenia research*, 83(2):155–171, 2006.
- [23] Susumu Mori, Setsu Wakana, Peter CM Van Zijl, and LM Nagele-Poetscher. Mri atlas of human white matter. 2005.
- [24] RW Cox, John Ashburner, Hester Breman, Kate Fissell, Christian Haselgrove, Colin J Holmes, Jack L Lancaster, David E Rex, Stephen M Smith, Jeffrey B Woodward, et al. A (sort of) new image data format standard: Nifti-1. *Human Brain Mapping*, 25:33, 2004.
- [25] Richard Szeliski. Image alignment and stitching: A tutorial. *Foundations and Trends® in Computer Graphics and Vision*, 2(1):1–104, 2006.
- [26] Peter J Basser, James Mattiello, and Denis LeBihan. Mr diffusion tensor spectroscopy and imaging. *Biophysical journal*, 66(1):259–267, 1994.
- [27] Luca Nanetti, Leonardo Cerliani, Valeria Gazzola, Remco Renken, and Christian Keysers. Group analyses of connectivity-based cortical parcellation using repeated  $k$ -means clustering. *Neuroimage*, 47(4):1666–1677, 2009.
- [28] Rolf Kötter, Claus C Hilgetag, and Klaas E Stephan. Connectional characteristics of areas in walker’s map of primate prefrontal cortex. *Neurocomputing*, 38:741–746, 2001.
- [29] Richard E Passingham, Klaas E Stephan, and Rolf Kötter. The anatomical basis of functional localization in the cortex. *Nature Reviews Neuroscience*, 3(8):606–616, 2002.
- [30] Konstantin Andreev and Harald Racke. Balanced graph partitioning. *Theory of Computing Systems*, 39(6):929–939, 2006.
- [31] Jianbo Shi and Jitendra Malik. Normalized cuts and image segmentation. *Pattern Analysis and Machine Intelligence, IEEE Transactions on*, 22(8):888–905, 2000.
- [32] Marina MeilPa and Jianbo Shi. Learning segmentation by random walks. 2001.
- [33] Ulrike Von Luxburg. A tutorial on spectral clustering. *Statistics and computing*, 17(4):395–416, 2007.

- [34] H. Lutkepohl. *Handbook of Matrices*. Wiley, 1997.
- [35] Arash A Amini, Aiyu Chen, Peter J Bickel, Elizaveta Levina, et al. Pseudo-likelihood methods for community detection in large sparse networks. *The Annals of Statistics*, 41(4):2097–2122, 2013.
- [36] Jiashun Jin. Fast network community detection by score. *arXiv preprint arXiv:1211.5803*, 2012.
- [37] John J Hopfield. Neural networks and physical systems with emergent collective computational abilities. *Proceedings of the national academy of sciences*, 79(8):2554–2558, 1982.
- [38] Erel Levine and Eytan Domany. Resampling method for unsupervised estimation of cluster validity. *Neural computation*, 13(11):2573–2593, 2001.
- [39] Aristides Gionis, Heikki Mannila, and Panayiotis Tsaparas. Clustering aggregation. *ACM Transactions on Knowledge Discovery from Data (TKDD)*, 1(1):4, 2007.
- [40] Charles T Zahn. Graph-theoretical methods for detecting and describing gestalt clusters. *Computers, IEEE Transactions on*, 100(1):68–86, 1971.
- [41] Hong Chang and Dit-Yan Yeung. Robust path-based spectral clustering. *Pattern Recognition*, 41(1):191–203, 2008.
- [42] Cor J. Veenman, Marcel J. T. Reinders, and Eric Backer. A maximum variance cluster algorithm. *Pattern Analysis and Machine Intelligence, IEEE Transactions on*, 24(9):1273–1280, 2002.
- [43] Anil K Jain and Martin HC Law. Data clustering: A users dilemma. In *Pattern Recognition and Machine Intelligence*, pages 1–10. Springer, 2005.
- [44] Limin Fu and Enzo Medico. Flame, a novel fuzzy clustering method for the analysis of dna microarray data. *BMC bioinformatics*, 8(1):3, 2007.
- [45] Robyn Honea, Tim J Crow, Dick Passingham, and Clare E Mackay. Regional deficits in brain volume in schizophrenia: a meta-analysis of voxel-based morphometry studies. *American Journal of Psychiatry*, 162(12):2233–2245, 2005.
- [46] Ernst Hellinger. Neue begründung der theorie quadratischer formen von unendlichvielen veränderlichen. *Journal für die reine und angewandte Mathematik*, 136:210–271, 1909.